The Dissertation Committee for Thomas Glenn Collier certifies that this is the approved version of the following dissertation:

Near Real Time Confocal Microscopy of *Ex Vivo* Cervical Tissue: Detection of Dysplasia

Committee:

Rebecca Richards-Kortum, Supervisor

Kenneth Diller

Michele Follen

Henry G. Rylander

Thomas Milner

Near Real Time Confocal Microscopy of *Ex Vivo* Cervical Tissue: Detection of Dysplasia

by

Thomas Glenn Collier, B.Arch., M.S. E. E.

Dissertation

Presented to the Faculty of the Graduate School of

The University of Texas at Austin

in Partial Fulfillment

of the Requirements

for the Degree of

Doctor of Philosophy

The University of Texas at Austin

December 2004

I dedicate this work to my wife, Debbie, whose patience and support made the completion of this project possible. Also to Grace and David who make life fun.

ACKNOWLEDGEMENTS

I would like to thank my advisor, Dr. Rebecca Richards-Kortum for her support, integrity and encouragement; Dr. Michele Follen and the research nurses for their help in acquiring the numerous biopsies required for this project; the members of my committee and my fellow students who made work fun. I'd also like to thank my Mom and Dad, Carroll and Mildred Collier, who always encouraged a curious mind.

Tom

Near Real Time Confocal Microscopy of *Ex Vivo* Cervical Tissue: Detection of Dysplasia

Publication No. _____

Thomas Glenn Collier, PhD

The University of Texas at Austin, 2004

Supervisor: Rebecca Richards-Kortum

Recent studies have shown the ability of confocal microscopy to non-invasively image cells *in vivo* in real time. This ability to visualize nuclei *in vivo* shows the potential of confocal microscopy to dramatically improve the prevention, detection and therapy of epithelial cancers. More exciting is the potential to quantitatively measure nuclear morphometry providing a basis to automate the cancer detection process. This dissertation describes studies exploring this potential in *ex vivo* cervical tissue using acetic acid as a nuclear contrast agent.

First the use of acetic acid was demonstrated to improved contrast in confocal images of cervical tissue sufficiently to allow segmentation. Segmentation is robust throughout the epithelium in most normal tissue and upper portions of tissue diagnosed with severe dysplasia. Based upon this segmentation, quantitative feature measurements were extracted from confocal images of

cervical tissue in a pilot study to determine if the features would aide in the detection of dysplasia. Simultaneously, a qualitative review of confocal images was performed by untrained reviewers and compared with clinical colposcopic impressions, the standard clinical tool aiding in dysplasia detection. The sensitivity and specificity of both the qualitative (95% and 69%) and quantitative (100% and 91%) review were improved compared to colposcopic review (91% and 62%).

Finally the ability of confocal microscopy to produce 3D images was explored as a further means to improve dysplasia detection. Based upon Beer's equation for light attenuation, the scattering coefficient was extracted from 3D image sets of *ex vivo* cervical tissue and compared with histology from the same precancerous lesion. The results suggested a possible correlation between high scattering values and the presence of dysplasia. Quantitative 3D features were also extracted from 3D image sets and correlated with the presence of CIN 2/3. Increased separation between normal and CIN 2/3 biopsies was produced using the 3D features as compared to the 2D. More importantly, when additional information (scattering coefficient) is combined with the 2D features, the ability to distinguish between normal and CIN 2/3 is 100% accurate in this small sample set.

TABLE OF CONTENTS

List of Figures

List of Tables

CHAPTER 1

Research Objectives

1.1 INTRODUCTION

Recent studies have shown the ability of confocal microscopy to non-invasively image cells *in vivo* in real time [1,2,3]. Melanin provides the contrast necessary to visualize cell structure in human skin [2], and acetic acid has been shown to provide the needed contrast to image nuclei deep within amelanotic epithelia [4]. This ability to visualize nuclei *in vivo* shows the potential of confocal microscopy to dramatically improve the prevention, detection and therapy of epithelial cancers. More exciting is the potential to quantitatively measure nuclear morphometry providing a basis to automate the cancer detection process. To date no studies have been performed to demonstrate this potential in cervical tissue. This dissertation describes four studies exploring this potential.

1.2 SPECIFIC AIMS

- **Aceto-whitening**

  Confocal imaging of amelanotic tissue contains inherently less contrast, but after the application of acetic acid, back scattering from nuclei becomes pronounced [4]. The first step in the quantitative identification of dysplasia in the cervix is to determine whether the contrast provided by acetic acid is sufficient to allow for morphometric measurements of nuclei, the primary organelle used by pathologists for

identifying dysplasia. The first aim was to determine if the increased contrast allowed automated nuclear segmentation and thus nuclear morphometry.

- **Detection of Dysplasia**

  If nuclear segmentation can be performed on confocal images, is the morphometric information provided useful for detecting dysplasia? Or are the images themselves qualitatively useful in identifying dysplasia? The second aim was to explore the ability of confocal imaging to provide sufficient qualitative and quantitative information to detect the presence of cervical dysplasia. Images were processed to extract nuclear morphometric information and qualitatively analyzed by a group of untrained reviewers. The information and opinions obtained were correlated with histopathologic review for the presence of dysplasia.

- **3D Morphology**

  The ability of confocal microscopy to acquire three-dimensional images offers another exciting possibility for acquiring additional information needed to aid in the detection of dysplasia. Three-dimensional imaging offers the potential to explore the architecture of the epithelia and to extract three-dimensional morphometry using the increased sampling provided. The third aim was to explore the three dimensional imaging of normal and dysplastic cervical tissue *ex vivo*. Morphometric and architecture measurements were correlated with the presence of dysplasia.

- **Extracting the Scattering Coefficient**

  Resent studies have shown evidence of a change in the scattering coefficient between normal and dysplastic tissue and suggests that extracting the scattering coefficient may aid in dysplasia detection [27, 78]. Extraction of the scattering coefficient from ex vivo cervical tissue would also provide valuable information to aid in tissue modeling. Accurate models are necessary to aid in the development of tissue classification algorithms used by optical diagnostic devises such as spectroscopy devises. The last aim was to use the information provided by three-dimensional confocal imaging to extract the scattering coefficient from cervical tissue.

1.3 BRIEF OUTLINE

The following Chapter provides background information on the cervix and confocal imaging. Chapter 3 describes the dynamics of aceto-whitening and tests if the contrast enhancement provided is sufficient for nuclear segmentation. Chapter 4 explores whether qualitative and quantitative information derived from 2D confocal microscopy can be used to detect dysplasia. Chapter 5 explores the use of confocal microscopy for extracting the scattering coefficient from various regions of the cervical epithelium. Finally Chapter 6 describes the use of 3D confocal imaging for the detection of dysplasia based upon qualitative review and quantitative features extracted from cervical tissue. A comparison with 2D confocal imaging is made, and the scattering information derived from Chapter 5 is used as an added feature in the detection of dysplasia.

CHAPTER 2

Background

2.1 INTRODUCTION

This chapter provides background in confocal microscopy and the anatomy of the cervix. The first section describes the motivation for the use of confocal microscopy to detect dysplasia. The next section provides information about the anatomy of the ecto-cervix which is the portion of the cervix studied. The last two sections provide information on confocal microscopy and a description of the confocal system developed to perform the research described in this proposal.

2.2 MOTIVATION

Cancers of the lining, or epithelium, of the cervix are preceded by precancerous cell growth within the epithelium. Mortality for the cancers is significant [5]. Current methods for the screening and detection of cervical cancers fall into three categories: 1) the examination of exfoliated cells (the Pap smear), 2) visual examination of the surface to identify abnormal areas (colposcopy) and 3) histological examination of biopsies. The first two are screening techniques while histology is only performed if the clinician sees a suspect area.

The predictive value of cytological screening is limited by sampling and reading error. The predictive value for cancer in cervix is better with visual

examination. For example, detection of cancer with colposcopy of the cervix has a sensitivity of 90%, however the specificity is poor since tissue inflammation is difficult to differentiate from cancer. This low specificity leads to a substantial number of unnecessary biopsies. The unnecessary biopsies are costly and painful, thus deterring patients from necessary follow-up clinical visits. Histological examination of biopsies is the gold standard of cancer detection; however its disadvantages include the necessity of tissue biopsy and time of preparation.

A non-invasive alternative is to image cells *in vivo* using reflected light from within the tissue. This approach is similar to histological analysis of biopsies with the added advantages of facilitating imaging at the clinic and 3D resolution can be achieved without removal of tissue. Confocal imaging can be used to localize the light in three dimensions with enough resolution to image individual cells. Changes in the index of refraction provide contrast to recognize intracellular detail. Detection of increased nuclear size, nuclear to cytoplasmic ratio and nuclear texture using confocal microscopy would yield sufficient information to diagnose neoplasia in a manner similar to histology.

2.3 ANATOMY OF THE ECTO-CERVIX

The ecto-cervix is the portion of the cervix which surrounds the external orifice or opening into the uterus. It is covered with a 100-500 μm thick epithelial tissue composed of stratified squamous cells. The surface of the epithelium is exposed to the immediate environment; the bottom is bound to a continuous basement membrane which separates the epithelium from stromal tissue. The stroma is composed primarily of collagen and elastin fibers and also

contains capillaries, nerves and fibroblast cells. The epithelium is avascular and receives most of its nutrients from extracellular fluid which perfuse through both the stromal fibers and between desmosomes on epithelial cells.

Cancers of the cervix and their precursors are often detected histologically by noticing changes in cell shape, nuclear morphology and tissue structure. Neoplasia, dysplasia and cancer are terms often used to describe these changes. Neoplasia is a general term used to describe an abnormal area of new cell growth. Dysplasia is used to describe areas of tissue with abnormal morphologic changes. These changes include atypical cell orientation and sizes, increased nuclear sizes, changes in nuclear texture, increased nuclear to cytoplasmic ratio, cell division outside the basement membrane and thickening of the epithelium, Figure 2. [6]. Dysplasia is also characterized as 1) CIN I (cervical intraepithelial neoplasia I), localized in the bottom third of the epithelium, 2) CIN II, localized in the bottom two thirds and 3) CIN III, covering the entire thickness. When the area of dysplasia breaks through the basement membrane it becomes a cancer and is able to spread to other parts of the body.

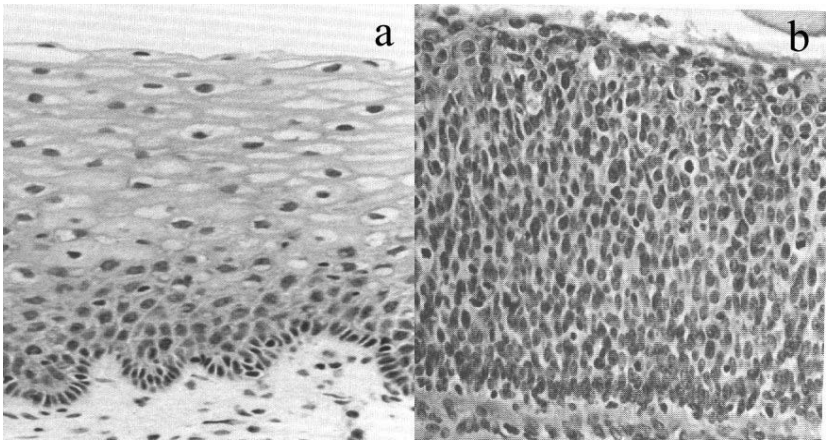

Figure 2.1. Epithelial dysplasia of the cervix. a.) Normal cervical epithelium showing typical differentiation from basal to squamous cells as they grow to the top of the epithelium. b.) Dysplasia is characterized here primarily by the lack of differentiation.

Cervical tissue is typically translucent in appearance; much of the light entering the tissue is scattered while little of it is absorbed. The sources of scattering from the epithelium are not well understood. It is postulated that varying index mismatches between cells and within cells between the cytoplasm and organelles, primarily the nucleus, may play an important role [7]. There is no dominant source of absorption within this epithelial tissue. Absorption by hemoglobin is not a factor since the epithelium is avascular.

2.4 CONFOCAL MICROSCOPY

Confocal microscopy is a technique of imaging tissue samples by optical sectioning. Optical sectioning makes it unnecessary to physically slice the sample thus leaving it undisturbed and making it possible to image below the surface of the tissue. Optical sectioning is performed by placing a pinhole aperture at a

conjugate image plane to the plane within the sample to be imaged, Figure 2.2. Light originating from the section of interest is focused through the pinhole to the detector while light originating from sections immediately above and below the section of interest is sufficiently blurred at the pinhole to be rejected. In this Figure, the source is reflected off the sample; however confocal microscopes can also use transmitted as well as reflected light.

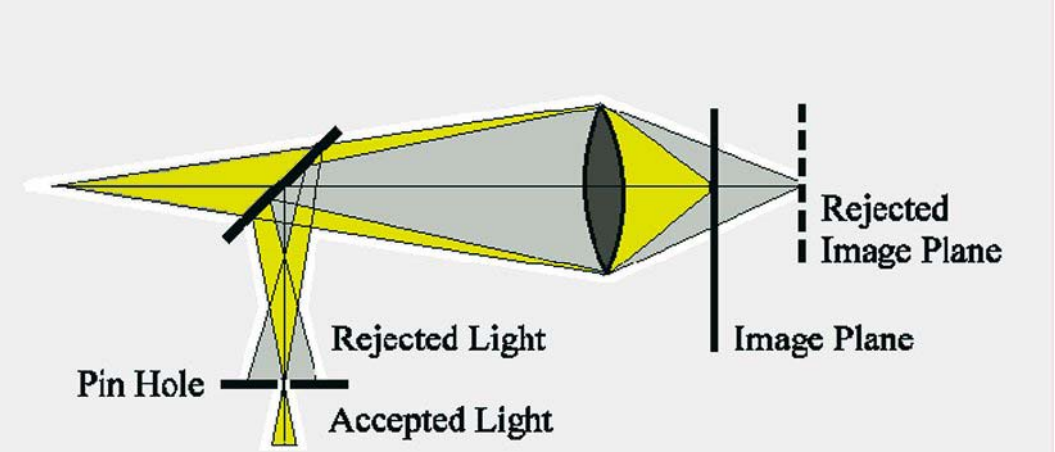

Figure 2.2. Schematic of the optical sectioning principle of confocal microscopy.

2.5 Axial and Lateral Resolution in Confocal Microscopy

The primary advantage of confocal microscopy is the improved axial resolution over bright field microscopy. The diffraction limited axial resolution for both bright field and confocal are the same in theory

$$Z = 2n\frac{\lambda}{(NAobj)^2}$$

where Z is the distance from the center to the first minimum in the diffraction pattern in the axial direction and n is the index between the objective and the sample. The axial resolution of bright field microscopy is much poorer than this in practice due to significant scattering which enters the field of view from above and below the focal plane. This scattering is exactly what the confocal pinhole removes.

The axial resolution in confocal microscopy also cannot reach the diffraction limit because of the finite size of the pinhole. The axial resolution equation assumes that the detector is infinitesimally small. The axial resolution of a confocal microscope using a finite radius pinhole can be modeled assuming an ideal plane object and using a general transfer equation for the lenses before the pinhole [8]. The equation for the transfer function is given by

$$h(u,v) = \int_0^1 P(\rho) \exp^{\frac{ju\rho^2}{2}} Jo(v\rho)\rho d\rho \qquad u = \frac{8\pi}{\lambda}[n\sin(\alpha/2)]^2 z$$

where u is the dimensionless axial coordinate, sin (α) is the NA of the lens to the pinhole, P(ρ) is the pupil function and J_o is a Bessel function of the 0^{th} order. The axial response to a plane reflective object is given by [8]

$$I(u) = \int_0^{v_p} \left|h(2u,v)\right|^2 v dv \qquad v_p = \frac{2\pi}{\lambda} r_p NA$$

where v_p is the normalized pinhole radius and r_p is the radius of the pinhole aperture. The solution for a few values of v_p were acquired from ref [8] and are shown in Figure 2.3. For values of $v_p < 2$ there is little observable difference from the ideal sectioning pinhole radius of 0. At $v_p = 4$, the pinhole is larger than

the airy diffraction disk and sectioning becomes noticeably poorer. In order to maintain good sectioning without reducing throughput, a v_p of 2.5 is recommended [8]. Using the calculated u_{fwhm} values from Figure 2.3, the axial resolution of the confocal microscope can be calculated as:

$$z_{fwhm} = \frac{u_{fwhm}\lambda}{4\pi M_T^2 \left[n \sin(\alpha/2)\right]^2}$$

where M_T is the transverse magnification of the system up to the pinhole lens. Typical values of z are sub-micron to a few microns.

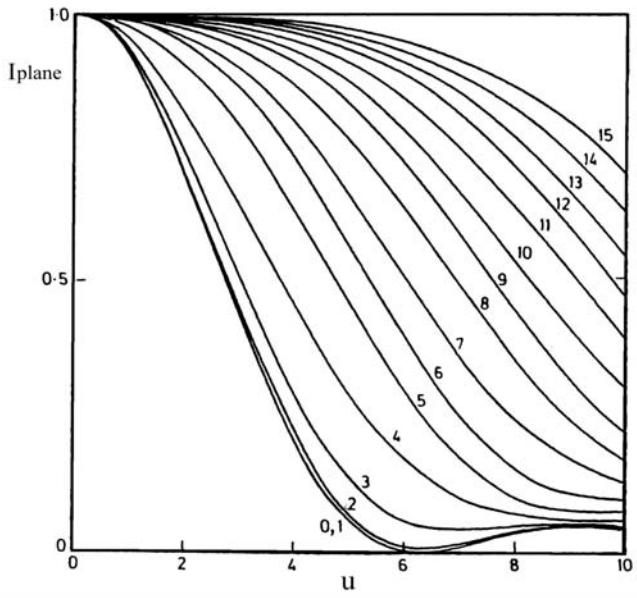

Figure 2.3. Model of the signal intensity from a plane reflector object versus u, the objects dimensionless axial position for numerous values of the v_p, the normalized pinhole radius.

The lateral resolution of confocal microscopy can also be improved over bright field. The lateral resolution is improved using a pinhole which is small compared to the diffraction limit of the lenses at the pinhole [8]. At these pinhole

sizes, however, throughput at the pinhole becomes limited because the pinhole begins to block light from the central maximum of the diffraction limited spot. At the optimum pinhole size with regard to throughput, the resolution is approximately the same as bright field, namely the diffraction limited resolution

$$R = 0.61\frac{\lambda}{NAobj}$$

where R is the distance from the center to the first minimum of the airy disk and NA_{obj} is the numerical aperture of the objective.

2.6 THE CONFOCAL SYSTEM

I developed the confocal microscope used in the studies described in Chapters 3 through 6. It was designed as a prototype for a near real time *in vivo* fiber optic confocal endoscope [9]. The system diagram is shown in Figure 2.4. The light source is a continuous wave diode laser operating at 810 nm in the studies described in Chapters 4-6 and a Ti-Sapphire laser in the study described in Chapter 3. The scanning mirrors are driven by a pair of galvanometers to produce the frame rate. The scanning lens (80 mm achromat doublet) focuses the beam at the back focal plane of a 25X 0.8 NA water immersion objective (Plan-Neofluar multi-immersion, Zeiss). 10-30 mW of power is focused to a 1 μm diameter spot on the sample. Light backscattered from the tissue returns to the beam splitter where it is reflected to the pinhole lens (50 mm achromat doublet) and focused through a 10 μm diameter pinhole aperture. Light which passes through this pinhole is collected by the collecting lens (50 mm achromat doublet) and detected

by an avalanche photodiode by Hamamatsu. The confocal system operates at a dimensionless pinhole radius of 2.5 to provide maximum optical sectioning for obtaining cellular detail. The scanning system is capable of scanning at variable angle ranges thus providing zoom capability. The measured lateral and axial resolution of the system are 0.8 μm and 3-5 μm respectively. The system was originally designed for a frame rate of 15 frames per second using a 15 Hz scanning system (8000 kHz Video Scan Head, General Scanning). The studies on acetic acid in Chapter 3 were performed at this frame rate. After a failure of the scanning system, the confocal microscope system was rebuilt with a 6.5 frame rate scan system (4000 kHz Video Scan Head, General Scanning). Changes in imaging depth are made by translating the sample stage up and down with a differential micrometer.

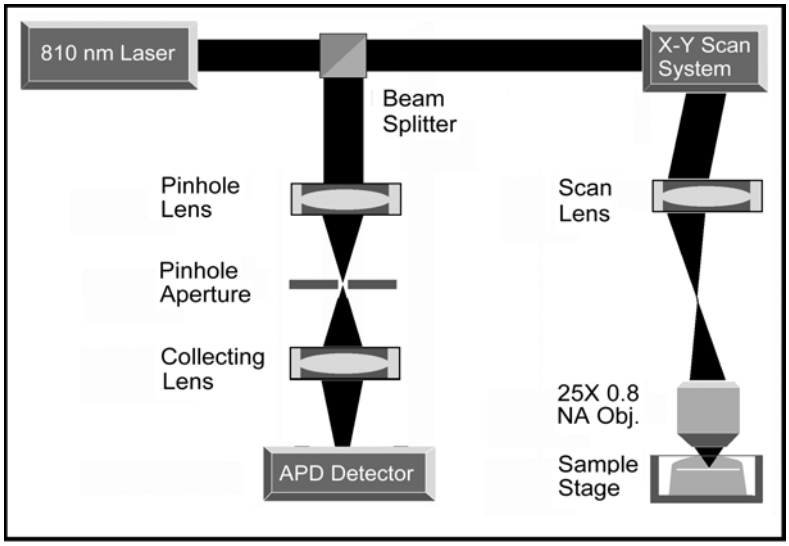

Figure 2.4 Confocal system diagram.

CHAPTER 3

Near Real Time Confocal Microscopy of Amelanotic Tissue: Dynamics of Aceto-Whitening Enable Nuclear Segmentation

This Chapter describes the exploration of the aceto-whitening in normal and neoplastic cervical tissue *in vitro* to determine whether sufficient contrast can be obtained to allow nuclear segmentation. The study has been previously published in Optics Express [10] and is reproduced here with limited non-substantive modifications.

3.1 INTRODUCTION

Cancers of the epithelium of the cervix, urinary bladder, respiratory tract, oral mucosa, skin and colon are preceded by precancerous changes within the epithelium. Despite the presence of pre-cursor lesions, mortality for these cancers is significant [11]. Early detection represents the best opportunity to improve patient survival and quality of life; thus, new surveillance methods are needed to improve the ability to recognize pre-cancerous changes within epithelial tissues. Epithelial pre-cancers are associated with a variety of morphologic alterations, including increased nuclear size, increased nuclear/cytoplasmic ratio, hyperchromasia and pleomorphism [12].

Confocal imaging has been proposed as a new tool to non-invasively assess cell morphology using light reflected from tissue [2, 13, 14, 16, 17, 15, 18]. A pinhole placed at a conjugate image plane in the confocal microscope is used to localize reflected light in three dimensions with sufficient resolution to image

individual cells and nuclei. Changes in refractive index provide contrast to recognize intracellular detail. In concept, this is similar to histological analysis of biopsy specimens, except three-dimensional resolution is achieved without removing or physically sectioning tissue. Thus, confocal imaging provides a potential tool to detect pre-cancerous changes in the intact epithelium

To date, much of the work using in vivo confocal imaging has focused on the eye [16,17,18] and skin [2,3] where melanin with its high refractive index (n=1.7) provides the primary source of contrast for imaging individual cells. Cervical tissue being amelanotic provides inherently less contrast for confocal imaging. [19] However, when tissue [4] is treated with weak acetic acid, the backscattering associated with the nucleus increases, providing additional contrast in confocal images. Acetic acid is commonly used to aid in the detection of cervical pre-cancer during cervical precancers [20]. Precancerous areas of the cervix turn whitish 2-3 minutes after the application of 3-6% acetic acid.

The goals of this study are to use confocal imaging to observe the time course of aceto-whitening at the cellular level and to determine whether the contrast provided enables quantitative feature analysis to quantitatively probe additional nuclear morphometry.

3.2 MATERIALS AND METHODS

3.2.1 Confocal System

We designed and built an epi-illuminaiton confocal microscope (Figure 3.1). The light source is a continuous wave argon-ion pumped Ti:Sapphire laser tuned to 808 nm (890 Tunable Laser, Coherent). The beam is spatially filtered

with a single mode optical fiber, collimated, and sent through a beam splitter to an x-y scanning system. The scanning mirrors are driven by a pair of galvanometers to produce a frame rate of 15 Hz (8000 kHz Video Scan Head, General Scanning). The scanning lens, L1, focuses the beam at the back focal plane of a 25X 0.8 NA water immersion objective (Plan-Neofluar multi-immersion, Zeiss). 10-30 mW of power is focused to a 1 μm diameter spot on the sample. Light backscattered from the tissue returns to the beam splitter where it is reflected to the pinhole lens, L2, and focused through a 10 μm diameter pinhole. Light which passes through this pinhole is detected by an avalanche photodiode. The confocal system operates at a dimensionless pinhole radius of 2.5 to provide maximum optical sectioning for obtaining cellular detail. The scanning system is capable of scanning at variable angle ranges thus providing zoom capability. The measured lateral and axial resolution of the system are 0.8 um and 2-3 um respectively.

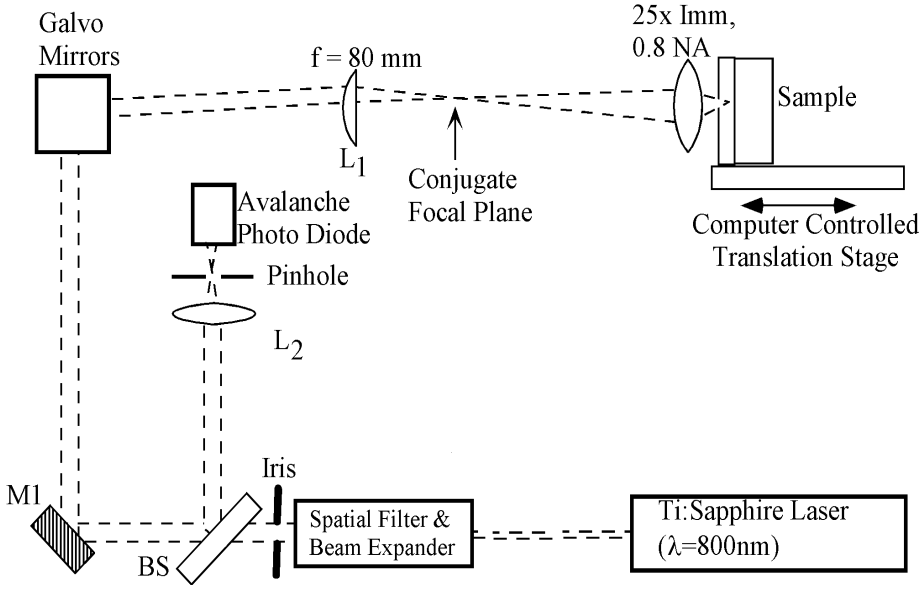

Figure 3.1. Set up of epi-illumination confocal microscope used to collect the images and video.

3.2.2 Specimens

Seven normal specimens of cervical tissue were obtained from seven patients following hysterectomy from the Southern Division of the Cooperative Human Tissue Network (CHTN) at The University of Alabama at Birmingham. The study was reviewed and approved by the Institutional Review Board at the University of Texas at Austin. One normal cervical biopsy was obtained from a patient undergoing colposcopy at the Colposcopy Clinic at the University of Texas M.D. Anderson Cancer Center. This patient was selected from a group of patients referred for follow-up colposcopy for suspected CIN on the basis of abnormal cervical cytology. Informed consent was obtained and the project was reviewed and approved by the Surveillance Committee at the University of Texas M.D. Anderson Cancer Center. The surgical samples were a minimum of 1 x 1 x 0.5 cm in size; the biopsy was 2-4 mm in size. All tissue specimens were frozen in liquid nitrogen immediately after collection and stored at -70°C until microscopic examination. Before imaging, each sample was thawed for 5-10 minutes in PBS.

3.2.3 Imaging

Confocal images were acquired from all eight samples before and after the application of acetic acid. Each biopsy was first imaged in PBS and image frames were acquired as the image plane was translated through various epithelial depths. A 6% solution of acetic acid was then added to each sample and image frames were acquired at various epithelial depths. Video was acquired from 2 of the 8 samples during and after addition of acetic acid. However, after addition of acetic

acid, tissue swelling occurred which prevented the focus from remaining at a fixed depth. A 6% solution of acetic acid in isotonic PBS was applied to a third sample to prevent the swelling and video was acquired during and after this addition. After acetic acid was applied, video was acquired from four of the samples as the focus of the microscope was moved from the epithelial surface down to 200 μm. In order to create a three-dimensional rendering of cell nuclei, images were obtained from two of the samples consecutively as the focus was moved at 1 μm intervals through two cell layers after application of acetic acid. The 1 μm interval was chosen to satisfy the Nyquist criteria for sampling with our system which has an axial resolution of 2-3 μm. All samples were submitted for routine histological analysis using hemotoxylin and eosin. An experienced, board certified gynecologic pathologist examined sections.

3.2.4 Image Processing

Each of the single frames presented here was resampled and processed to enhance the brightness and contrast. The brightness and contrast were increased by 22% and 53% respectively on each image taken before acetic acid, and 17% and 53% on each image taken after acetic acid. Brightness was enhanced by adding the noted percentage of full gray scale to each pixel; contrast was enhanced by removing the noted percentage of full gray scale from the image and expanding the remaining midrange gray levels. Resampling was performed to reduce the distortion in the images caused by nonlinearity in the resonant galvonometric scanning system. Linear interpolation was used to estimate pixel values. The three dimensional rendering of the incremental image slices was

performed using standard 3D surface rendering. Before rendering, the images were median filtered and thresholded to remove noise and smaller elements of the cells.

A feature detection algorithm was developed to detect and outline the cell nuclei, based on mathematical morphology, using a modification of the approach of Thiran [21]. This process consists of four steps. In the first, the image is thresholded to reduce noise and converted from grayscale to binary. Then the image is closed and then opened using flat, square structuring elements in order to remove all objects smaller than the nuclei. Next, the image is reconstructed using geodesic dilation to preserve the original shape of the nuclei. The reconstructed image is then closed again using a flat, square-structuring element to reduce texture within the nucleus. Finally, the edges are identified to yield the nuclear contours. Twelve images from eight samples were processed with this algorithm. Eight of the images were of tissue treated with acetic acid; four were obtained pre-acetic acid. Brightness and contrast were not enhanced on any image before processing. The images were resampled as described above after processing.

3.3 RESULTS

Figure 3.2 shows images of the tissue before acetic acid was applied. The cell outlines and nuclei can be clearly seen in most cells imaged near the epithelial surface (Fig 3.2a). As the focus is moved deeper, near the middle of the epithelium, the cell outlines can still be seen, but reflections from the nuclei are faint (Fig 3.2b). Most intra-cellular detail is lost in images taken near the bottom of the epithelium (data not shown). Figure 3.3 shows images taken after the

application of acetic acid. Near the tissue surface the cell outlines are less visible, but the nuclei are dramatically brighter (Fig 3.3a). In the middle of the epithelium, the nuclei can still be clearly seen (Fig 3.3b). As the focus is moved near the bottom of the epithelium, 200 μm below the epithelial surface, the nuclei are faint but visible in the smaller cells near the basement membrane (Fig 3.3c).

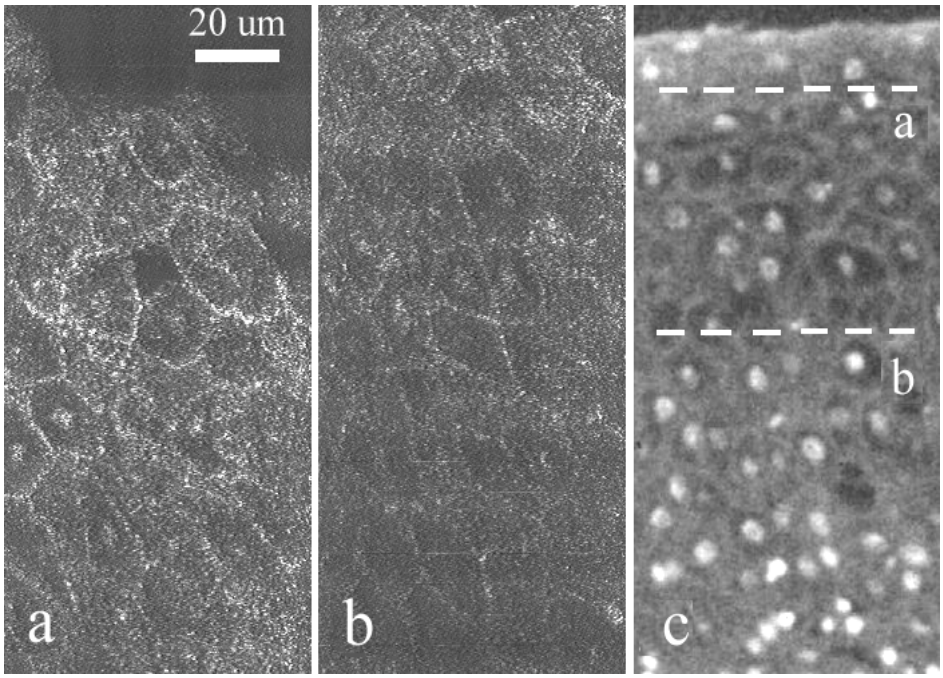

Figure 3.2 Images of cervical biopsy obtained prior to the application of acetic acid. a). Image taken with confocal microscope with the image plane parallel to the epithelial surface and the focus 20 microns below the surface. b). Same as (a), but with the focus 100 microns below the surface. c). Image of hemotoxylin and eosin stained transverse section using bright field microscopy. Contrast has been reversed in this black and white image to aid in comparing confocal and histologic images. Lines a and b indicate the approximate depth at which the confocal images in (a) and (b) were obtained.

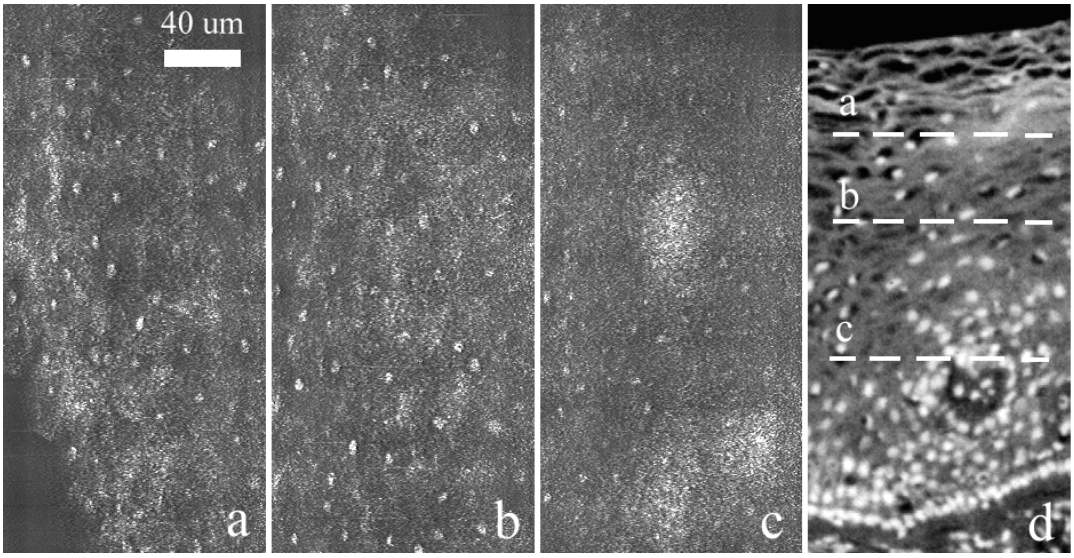

Figure 3.3 Images of cervical biopsy obtained after the application of acetic acid. a). Image taken with confocal microscope with the image plane parallel to the epithelial surface and the focus 50 microns below the surface. b). Same as (a) but with the focus 100 microns beneath the surface. c). Same as (a) but with the focus 200 microns beneath the surface. d). Image of hemotoxylin and eosin stained transverse section using bright field microscopy. Contrast has been reversed in this black and white image to aid in comparing confocal and histologic images. Lines a, b and c indicate the approximate depth at which the confocal images in (a), (b) and (c) were obtained.

While these images were obtained from tissue which was previously frozen, confocal images of fresh cervical tissue show similar morphologic features, pre and post acetic acid.

Samples from video (Figure 3.4) illustrate the dynamic changes in nuclear backscattering as acetic acid is applied to the sample surface. (The video can be seen in [10].) Here, the image plane of the microscope was fixed 50 μm beneath the epithelial surface, and the changes in image brightness and contrast are a result of the application of acetic acid; the field of view of each image is 150 μm.

Nuclei, which are barely visible before the application of acetic acid, can clearly be seen afterwards, and the increase in nuclear backscattering is rapid following addition of acetic acid. Through image processing, nuclei can be isolated in three dimensions. Figure 3.5 shows a three dimensional rendering created from multiple images taken at higher zoom through a small field of nuclei; the field of view is 100 μm. (Again, the video can be seen in [10])

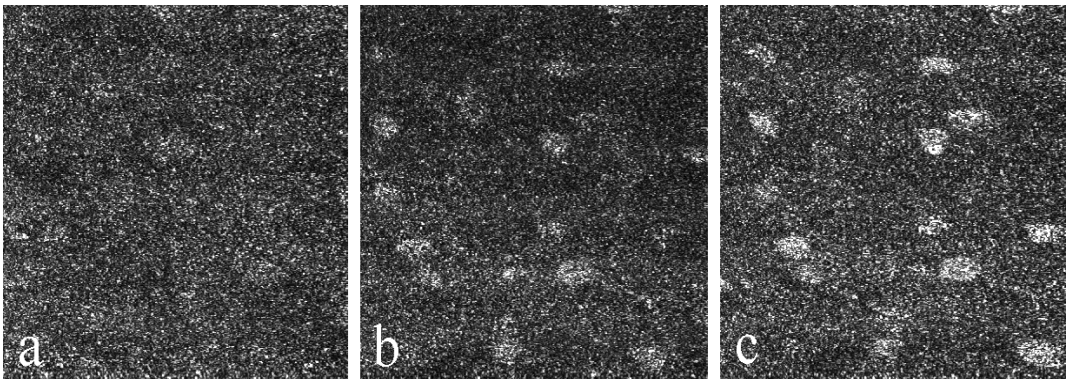

Figure 3.4. The time course of acetic acid. Little contrast is evident in the image taken without acetic acid, a. At 10 seconds nuclei become visible, b. At 20 seconds through the end of imaging, the contrast has reached its limit, c.

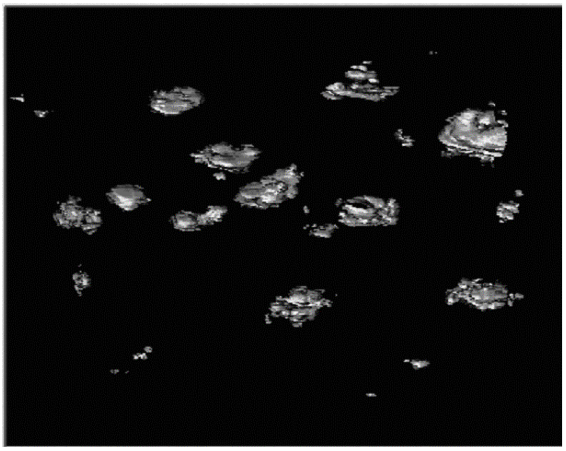

Figure 3.5 Three-dimensional rendering of the cervical tissue after the application of acetic acid.

The feature detection algorithm was applied to the images obtained before and after acetic acid to segment cell nuclei. For images acquired without acetic acid, features corresponding to nuclei, cell borders and noise were detected. (Fig 3.6). In images obtained after application of acetic acid, only nuclei were detected, and the nuclei were more accurately segmented. (Fig 3.7).

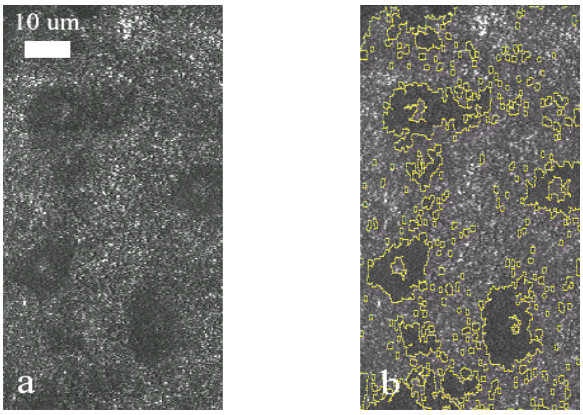

Figure 3.6 Segmentations of cell features with the feature detection algorithm on images taken without application of acetic acid. a). Unprocessed image. b). Same image as (a) with features outlined in yellow.

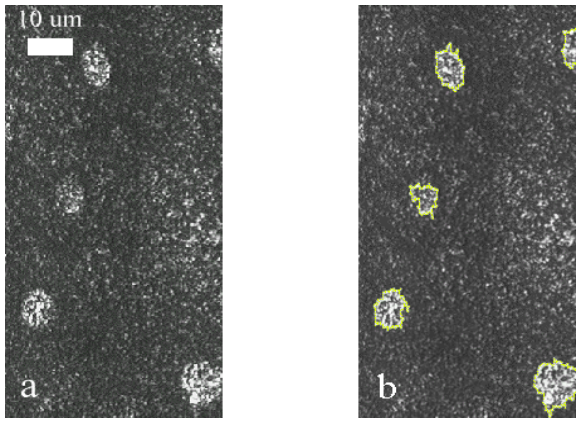

Figure 3.7 Segmentation of cell nuclei with our feature detection algorithm on images taken with the use of acetic acid. a). Unprocessed image. b). Same image as (a) with nuclei highlighted in yellow.

3.4 DISCUSSION AND CONCLUSIONS

These results show that acetic acid rapidly increases the backscattering of cell nuclei in cervical tissue *in vitro* resulting in confocal images with increased contrast. Within seconds after the application of acetic acid, nuclei can be visualized throughout the entire epithelium. The resulting image contrast is sufficient to enable nuclear segmentation and render nuclei in three dimensions. The feature detection algorithm was not robust in segmenting the nuclei however. For each image, a different threshold value was chosen to produce the presented results. Further work is needed in selecting the best suited threshold so that the process may be automated.

With further processing of the images, these results show that it is possible to assess cell and tissue morphometry quantitatively, for example the nuclear/cytoplasmic ratio and nuclear deformity can be calculated [21]. These results suggest that confocal imaging following application of acetic acid may prove to be a useful tool in recognition of epithelial precancers since precancers are characterized by increased nuclear size, increased nuclear/cytoplasmic ratio, hyperchromasia and pleomorphism, which currently can only be assessed through biopsy. This method could be easily implemented clinically since acetic acid is already used in routine clinical examination of the cervix using colposcopy.

Many epithelial sites at risk for development of precancers are located in other areas of the body such as the bladder or lung which can be accessed with fiber optic endoscopes but not with conventional confocal microscopes. To access these sites, several fiber optic confocal microscopes have been developed

[22,23,24,25,26] however all suffer from a lack of reflected light to provide sufficient contrast *in vivo*. The acetic acid technique described here shows the potential to increase the backscattered light necessary which may improve the S/N ratio of these fiber optic confocal endoscopes.

CHAPTER 4

Part 1 - Near Real Time Confocal Microscopy of Amelanotic Tissue: Detection of Dysplasia in Ex-Vivo Cervical Tissue

This Chapter describes the ability of confocal imaging to detect cervical dysplasia *ex vivo* both by automated means and by qualitative review of confocal images by untrained reviewers. The study has been previously published in Academic Radiology [27] and is reproduced here with limited non-substantive modifications.

4.1.1 INTRODUCTION

Invasive carcinomas of the uterine cervix, urinary bladder, respiratory tract, oral mucosa, skin and colon are preceded by precancerous changes within the epithelium. Despite the presence of precursor lesions, mortality for these cancers is significant [11]. Early detection represents the best opportunity to improve patient survival and quality of life; thus, new surveillance methods are needed to improve the ability to recognize precancerous changes within epithelial tissues. Epithelial pre-cancers are associated with a variety of morphologic alterations, including increased nuclear size, increased nuclear/cytoplasmic ratio, nuclear hyperchromasia and pleomorphism [28].

Confocal imaging has been proposed as a new tool to non-invasively assess cell morphology using light reflected from tissue, [2, 29, 30, 16, 17, 31, 18]. A pinhole placed at a conjugate image plane in the confocal microscope is used to localize reflected light in three dimensions with sufficient resolution to image individual cells and nuclei. Changes in refractive index provide contrast to

recognize intracellular detail. In concept, this is similar to histological analysis of biopsy specimens, except three-dimensional resolution is achieved without removing or physically sectioning tissue. Thus, confocal imaging provides a potential tool to detect precancerous changes in the intact epithelium. Confocal images can also be acquired in near real time thus enhancing its potential use in a clinical setting for directing biopsy acquisition.

To date, much of the work using *in vivo* confocal imaging has focused on the eye [32,33,34] and skin [2,3]; organ sites which are easily accessible with fixed conventional microscopes. Our group is developing a fiber optic confocal endoscope (FOCE) for *in-vivo* imaging of less accessible organs such as the uterine cervix [9]. The system has been designed to image subcellular detail of these amelanotic tissues for *in-situ* detection of pathology. A fiber optic imaging bundle is incorporated into the system to provide the necessary flexibility for imaging organ sites not accessible to conventional confocal systems.

The most promising use for real-time confocal systems has been imaging human skin where melanin with its high refractive index (n=1.7) provides the primary source of contrast for imaging individual cells. [2]. We have previously shown [35, 4, 19] that confocal images of amelanotic cells have inherently less contrast than those of cells with melanin. However, when epithelial cells [35] and previously frozen tissue [4, 10] are treated with weak acetic acid, the backscattering associated with the nucleus increases, providing additional contrast in confocal images sufficient for quantitative nuclear morphometry [10]. Acetic acid is commonly used to aid in the detection of cervical precancer [20].

To assess the potential of the FOCM for *in-vivo* pathology detection we explore here whether confocal images of fresh cervical biopsies could be used to identify the presence of cervical precancer using a near real-time non-fiber prototype system. We report results of a pilot study using our near real-time confocal microscope; images of paired colposcopically normal and abnormal biopsies were obtained from 25 patients. Images were analyzed in two methods and results compared to histologic diagnosis. First, we compared quantitative cell features measured from the confocal images with histopathologic diagnosis for dysplasia by a board certified pathologist with expertise in gynecologic pathology. Second, we compared the same diagnosis with a qualitative review of the confocal images by 15 individuals with no formal pathology training. We find that sensitivity and specificity for detection of CIN II/III to be high (sensitivity=100%, specificity=91%), suggesting that real time confocal imaging may be useful for in vivo detection of cervical precancer.

4.1.2 METHODS AND MATERIALS

4.1.2.1 Patients

Cervical biopsies were acquired from twenty-five patients at the colposcopy clinics of the University of Texas M.D. Anderson Cancer Center, Herman Hospital and Lyndon Baines Johnson Hospital in Houston, Texas. The patients had been referred to these clinics for suspected dysplasia on the basis of an abnormal cervical cytology or for removal of the cervical tissue using the loop electrical excision procedure (LEEP) due to a previous diagnosis of dysplasia. Informed consent was obtained from the patients, and the project was reviewed and approved by the Surveillance Committee at the University of Texas M.D.

Anderson Cancer Center and the Institutional Review Board at the University of Texas at Austin. Five patients were removed from the study due to unsuccessful acquisition or histologic processing of one of the two biopsies. An additional patient, with only focal dysplasia on histological examination on one of the biopsies, was removed from the study because it was felt that the probability of a meaningful correlation between the histologic diagnosis and the confocal images was remote.

4.1.2.2 Confocal System

We designed and built an epi-illuminaiton confocal microscope [19] (Figure 4.1). The light source is a continuous wave diode laser operating at 810 nm. The scanning mirrors are driven by a pair of galvanometers to produce a frame rate of 6.5 Hz (4000 kHz Video Scan Head, General Scanning). The scanning lens focuses the beam at the back focal plane of a 25X 0.8 NA water immersion objective (Plan-Neofluar multi-immersion, Zeiss). 10-30 mW of power is focused to a 1 μm diameter spot on the sample. Light backscattered from the tissue returns to the beam splitter where it is reflected to the pinhole lens and focused through a 10 μm diameter pinhole aperture. Light which passes through this pinhole is detected by an avalanche photodiode. The confocal system operates at a dimensionless pinhole radius of 2.5 to provide maximum optical sectioning for obtaining cellular detail. The scanning system is capable of scanning at variable angle ranges thus providing zoom capability. The measured lateral and axial resolution of the system are 0.8 um and 2-3 um respectively.

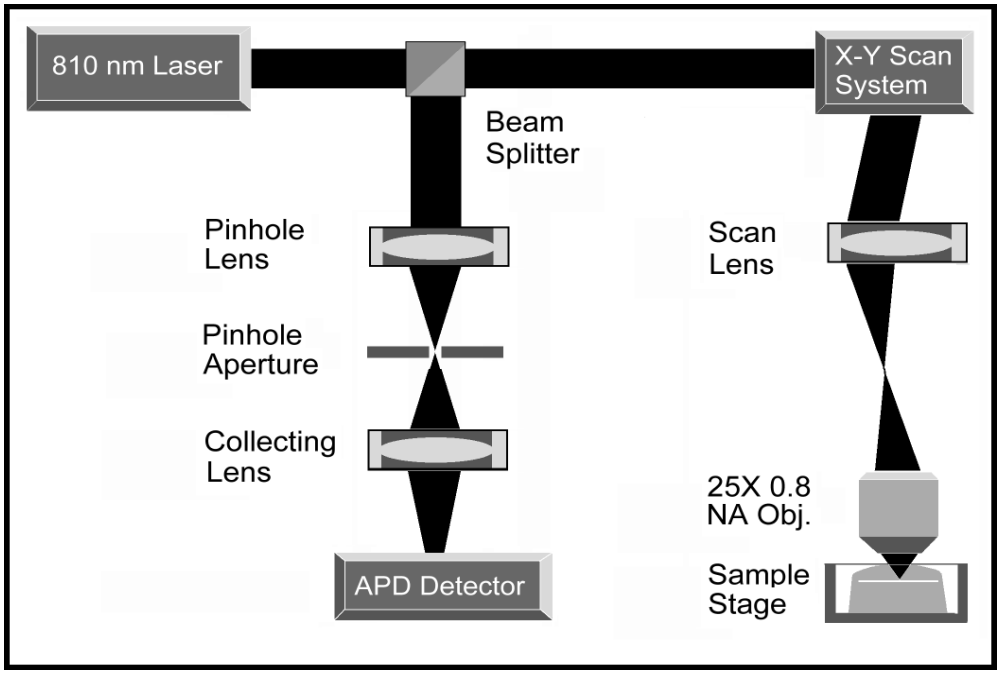

Figure 4.1 Confocal microscope system diagram.

4.1.2.3 Specimens

Two uterine cervix biopsies were acquired from each patient. One of the biopsies was taken from a normal area and the other was taken from an abnormal area of the cervix as determined by the clinician using colposcopy and immediately placed in growth media (DMEM, no phenol). Colposcopic impression (normal/abnormal) was recorded for each biopsy. The biopsies were approximately 3 mm wide by 4 mm long by 2 mm thick. Images were taken of the biopsies within 6 hours of excision.

4.1.2.4 Imaging

The biopsies were removed from the growth media and rinsed with PBS. A 6% solution of acetic acid was then added to each sample and image frames

were acquired at various epithelial depths up to the working distance of the microscope, 250 um. Confocal images were acquired with the image plane placed parallel to the tissue surface. Images were digitized using a video frame grabber card and displayed at 7.5 frames per second on a computer monitor. Individual bitmap image files were saved from the frame grabber's video buffer. All samples were submitted for routine histologic examination using hemotoxylin and eosin stain. Sections were examined by an experienced, board certified gynecologic pathologist (AM).

4.1.2.5 Image Processing

Each of the single frames presented here was resampled and processed to enhance the brightness and contrast. The brightness and contrast were increased by 17% and 53% respectively. Brightness was enhanced by adding the noted percentage of full gray scale to each pixel; contrast was enhanced by removing the noted percentage of full gray scale from the image and expanding the remaining midrange gray levels. Resampling was performed to reduce the distortion in the images caused by nonlinearity in the resonant galvonometric scanning system. Linear interpolation was used to estimate pixel values. Morphologic nuclear features including nuclear area, nuclear diameter, nuclear density and nuclear-to-cytoplasmic (N/C) ratio were extracted from each image. Nuclear masks were created by visual recognition of one operator blinded to the histologic and colposcopic results using a paint program. The images and masks were analyzed together with a feature measurement algorithm that was written using Labview (National Instruments) image processing tools. Statistical analysis

of the feature measurements were likewise performed using the tools available with Labview.

4.1.2.6 Pathologic review of the Confocal Images

Multiple confocal images at various depths were reviewed by 13 engineering graduate students and 2 biomedical engineering faculty from the University of Texas at Austin and the University of Texas M.D. Anderson Cancer Center. The review was performed in order to assess whether individuals with no formal training in pathology can make diagnosis of dysplasia from confocal images. Each reviewer was asked to diagnose each biopsy as normal or abnormal based on a training set of cervical confocal images taken from a previous study (14). Between 3 and 8 images per biopsy were grouped into image sets. The reviewer knew from which patient each image set came but was blinded to histologic diagnosis and colposcopic impression. Reviewers were informed that one biopsy from each patient was obtained from a colposcopically normal site and one from a colposcopically abnormal site, but that the histopathologic diagnoses of the pair could identify both as normal, both as abnormal or one abnormal and one normal. The sensitivity and specificity of each reviewer's diagnosis was calculated, using histopathology as the gold standard. Similarly, the sensitivity and specificity of the colposcopic impression were calculated.

4.1.3 RESULTS

Figure 4.2 shows images taken of the colposcopically normal and abnormal biopsies from one patient at various depths. The cell nuclei can be seen in all of the confocal images and the cell outlines can be seen around most cells of the normal biopsy. The nuclear density in the images taken from the abnormal

biopsy is clearly increased as compared to the images taken from the normal biopsy. The area of individual nuclei in the images from the abnormal biopsy is also greater than that of the normal biopsy. These differences, being evident at the top of the biopsies, suggest the presence of CIN III in the abnormal biopsy. The pathologic review of the abnormal biopsy confirmed this diagnosis. The maximum depth at which images could be obtained (penetration depth) also differed between this normal and abnormal biopsy. This is likely due to differences in scattering of light both to and from the image plane. The image of the abnormal biopsy (fig. 2j) taken at 125 um below the surface is the deepest at which subcellular detail can been visualized in this biopsy, however subcellular detail can still be visualized in images of the normal biopsy taken up to a depth of 250 um (not shown). This difference in scattering between normal and abnormal tissue could potentially provide another quantifiable measurement of contrast between normal and dysplastic tissue.

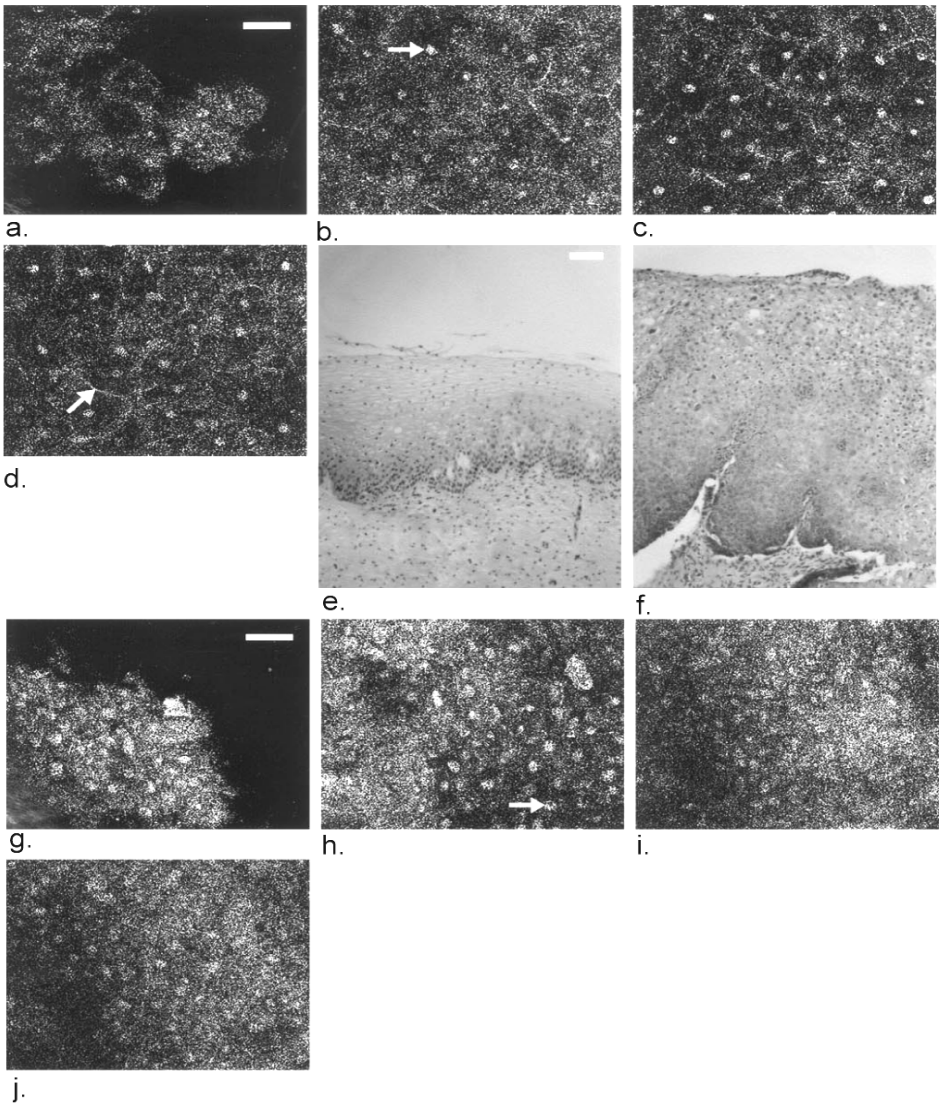

Figure 4.2. Images from a normal / abnormal biopsy pair from Patient 19. The confocal images of the colposcopically normal sample were taken 10 μm(a), 50 μm (b), 100 μm (c) and 150 μm (d) below the surface. The confocal images of the colposcopically abnormal sample were taken 10 μm(g), 50 μm (h), 100 μm (i) and 125 μm (j) below the surface and indicate increase nuclear size and density. Nuclei can be seen in all images (arrow b,h) and the cell outline can be seen in the normal sample (arrow d). Imaging depth in the abnormal sample was limited because of higher scattering. The increased nuclear size and density can be seen in the histologic image of the abnormal sample (f) over the normal (e). The scale bar in the confocal images is 50 μm wide and 100μm in the histology images.

Figure 4.3 shows image pairs taken from several patients and the corresponding histologic slide. In this case, all confocal images shown are from 50 um below the surface. In each biopsy pair, the difference in nuclear density and area is evident between the colposcopically normal and abnormal biopsy. The change in nuclear density between the normal and abnormal confocal image pairs is highlighted due to the orientation of the confocal images, which are perpendicular to those of typical histologic sections. Architectural similarities are also evident between the confocal and histologic images particularly in the images of dysplastic squamous epithelium that has involved a gland (fig. 3c-d). In this one confocal / histology pair the image orientation is the same.

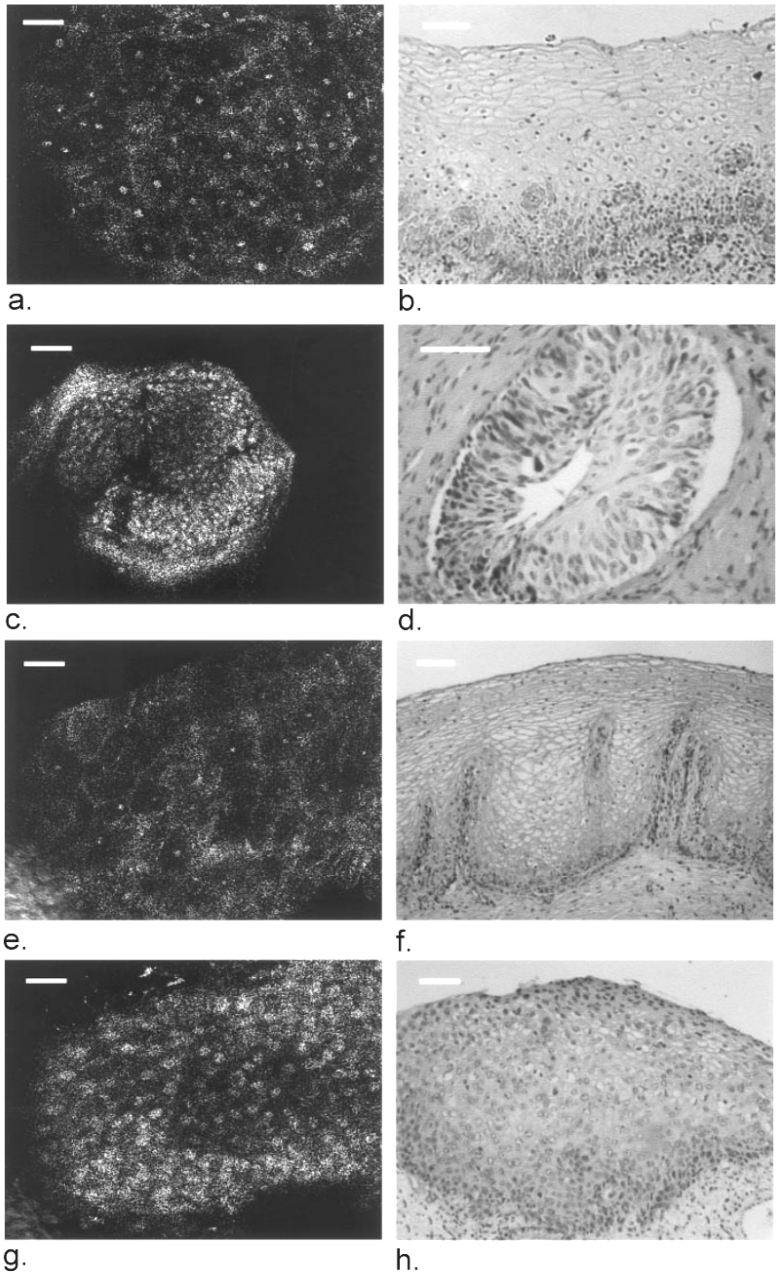

Figure 4.3. Images from normal / abnormal biopsy pairs from Patient 9 (a-d) and 12 (e-h). Increased nuclear density can be seen in the confocal images of the abnormal samples (c, g). The confocal images were taken 50 μm below the surface. The histologic images were classified as normal (b, f) and CIN II/III (d, h). The scale bars in the confocal images are 50 μm wide, 100μm in the histology images.

We reviewed the nuclear morphometric measurements extracted from the confocal images to determine whether any diagnostic contrast can be realized, and if so which features are most significant. Figure 4.4 shows a scatter plot comparing the average nuclear area from each biopsy with the nuclear / cytoplasmic (N/C) ratio from the same image. Each image was obtained 50 μm below the biopsy surface. A grouping of the normal and CIN I biopsies is clearly localized in the lower left quadrant. A distinction between normal and CIN I biopsies and biopsies with CIN II and II can be observed between N/C ratios below and above 0.08. No clear division line can be drawn to segment these

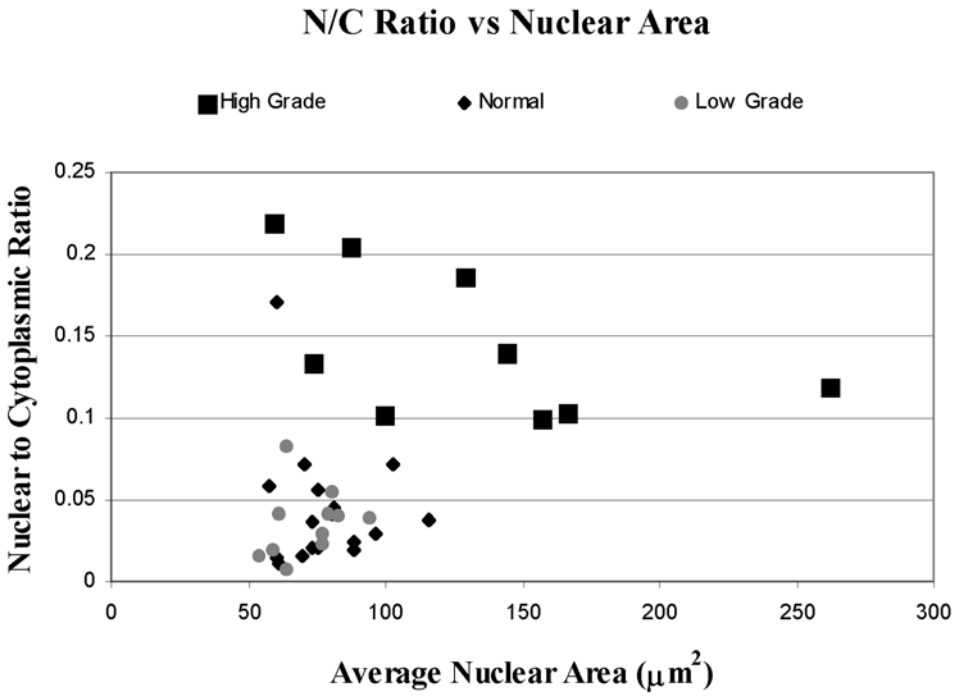

Figure 4.4. A comparison of the nuclear-to-cytoplasmic (N/C) ratio to the average nuclear area for biopsies categorized into three classes by pathologic review: normal, CIN I and CIN II/III. Measurements were calculated from images taken 50 μm below the tissue surface. Normal and CIN I samples are localized to the area with lower N/C ratio and lower nuclear area. The distinction between classes made by N/C ratio is better than that made by nuclear area.

classes according to nuclear area. While both features, nuclear area and N/C ratio, appear to contribute to the distinction between samples, types. The N/C ratio is clearly better at differentiating the two classes. The N/C ratio was also better at differentiating the tissue classes than nuclear density (not shown)

Figure 4.5 shows the average N/C ratio for all biopsies as a function of image depth within the biopsy. The error bar at each data point is a measure of two times the N/C ratio standard deviation for images at that depth. A clear division can be seen between biopsies diagnosed as CIN II/III and those diagnosed as CIN I or normal. If the biopsies with N/C ratios above 0.08 are categorized as CIN II/III, those below the ratio as CIN I or normal and these measurements are compared with the pathology results, the sensitivity and specificity of this classification method is 100% and 91% respectively.

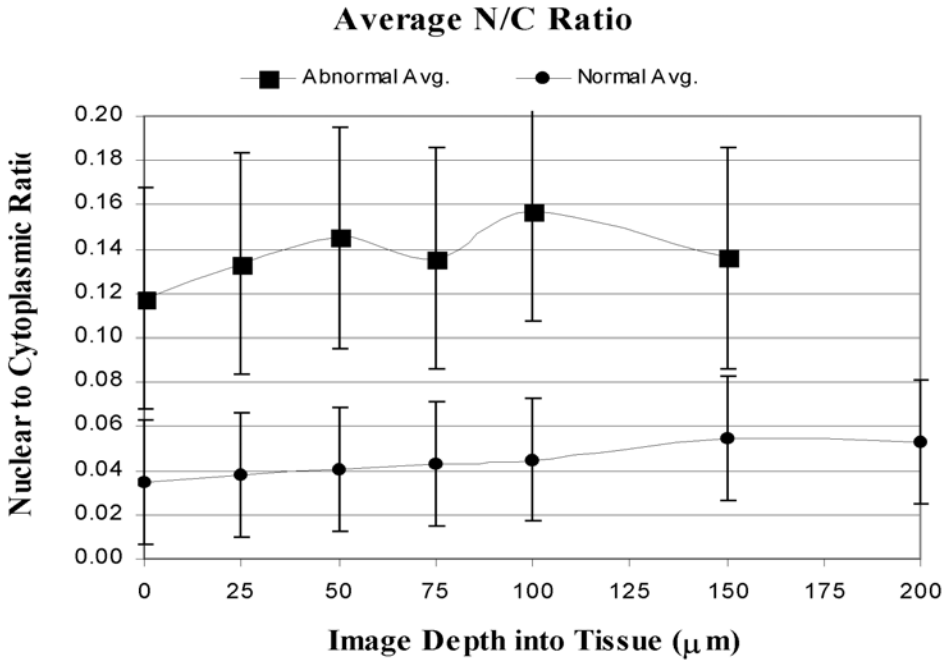

Figure 4.5. The nuclear-to-cytoplasmic ratio as a function of depth for biopsies categorized into two classes by pathologic review: normal or CIN I and CIN II/III.

Figure 4.6 shows the results of the diagnoses made by the untrained reviewers. The average sensitivity and specificity are 95% and 69% respectively. Sixty–four percent of the reviewers classified samples with a sensitivity of 100% with the remainder at 89%. The specificity varied from 50-76% with a standard deviation of +/- 8%. No reviewer approached the sensitivity and specificity of the quantitative analysis. The sensitivity and specificity of colposcopic impression compared to histopathologic diagnosis were 91% and 62%, respectively. The colposcopic and histopathologic diagnoses of the patient biopsies are shown in Table 1. Biopsies with a pathological diagnosis of inflammation and metaplasia were classified as normal in the sensitivity / specificity calculations; biopsies with a pathological diagnosis of koilocytosis were classified in this study with the CIN I biopsies.

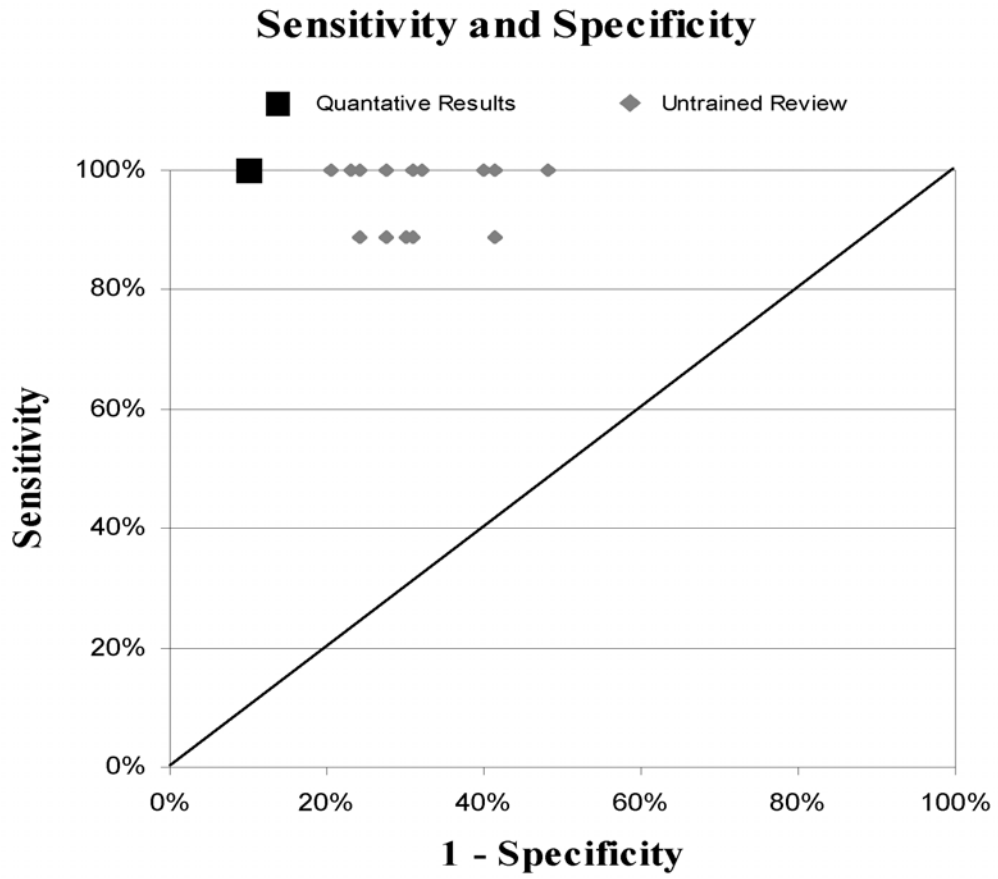

Figure 4.6. Sensitivity and Specificity for the diagnoses made by the untrained reviewers and quantitative analysis of the N/C ratio. The average sensitivity and specificity of the untrained reviewers (95% and 69% respectively) are an improvement over colposcopy. The sensitivity and specificity made by quantitative analysis is better (100% and 91% respectively).

Table 4.1 – Colposcopic impression and histopathologic diagnosis for each patient biopsy

Patient Diagnosis		
Patient Biopsy No.	**Colposcopic Impression**	**Histopathologic Diagnosis**
Biopsy 1A	Abnormal	Metaplasia
Biopsy 1B	Normal	Normal

Biopsy 2A	Normal	Normal
Biopsy 2B	Abnormal	Normal
Biopsy 3A	Abnormal	Koilocytosis
Biopsy 3B	Normal	Koilocytosis
Biopsy 4A	Abnormal	Koilocytosis
Biopsy 4B	Normal	Normal
Biopsy 5A	Normal	Normal
Biopsy 5B	Abnormal	CIN I
Biopsy 6A	Normal	Normal
Biopsy 6B	Abnormal	Metaplasia
Biopsy 7A	Normal	Normal
Biopsy 7B	Abnormal	CIN I
Biopsy 8A	Abnormal	Koilocytosis
Biopsy 8B	Normal	Koilocytosis
Biopsy 9A	Normal	Normal
Biopsy 9B	Abnormal	CIN II
Biopsy 10A	Abnormal	CIN II
Biopsy 10B	Normal	CIN I
Biopsy 11A	Normal	Normal
Biopsy 11B	Abnormal	Cancer
Biopsy 12A	Abnormal	Inflammation
Biopsy 12B	Normal	Normal
Biopsy 13A	Normal	Koilocytosis
Biopsy 13B	Abnormal	Koilocytosis
Biopsy 14A	Abnormal	CIN II
Biopsy 14B	Normal	CIN I
Biopsy 15A	Abnormal	Invasive carcinoma
Biopsy 15B	Normal	High grade dysplasia

Biopsy 16A	Normal	Normal
Biopsy 16B	Abnormal	CIN II
Biopsy 17A	Abnormal	Metaplasia
Biopsy 17B	Normal	Metaplasia
Biopsy 18A	Abnormal	CIN II/III
Biopsy 18B	Normal	Normal
Biopsy 19A	Normal	Normal
Biopsy 19B	Abnormal	CIN II/III

4.1.4 DISCUSSION

The pilot results here show that both quantitative analysis of confocal images and qualitative review by untrained observers can yield high sensitivity and specificity compared to histopathologic diagnosis. Analysis of nuclear feature measurements indicates that the N/C ratio appears to be the most important feature for detecting dysplasia using confocal images in which the image plane is parallel to the tissue surface. The penetration depth at which images with clear intracellular features could be obtained was limited to the upper half of the epithelium in biopsies with high-grade dysplasia, however we were still able to make accurate diagnoses of these biopsies.

To our knowledge, the high sensitivity and specificity of the system measured quantitatively are extremely promising and exceed most values reported from systems designed for *in vivo* detection of dysplasia. Furthermore, the qualitative analysis of the confocal images by the untrained reviewers provides an improvement over the macroscopic review of the tissue using colposcopy. The

sensitivity and specificity of colposcopy for this study are 91% and 62% respectively, which are higher than numbers previously published [36]. The 69% specificity of the untrained reviewers is also likely lower than might be measured with a more evenly distributed population of normal and abnormal biopsies. Many more biopsies were diagnosed by the pathologist as normal (29) than abnormal (9). This most likely resulted in a bias in the untrained reviewers toward increased false positives thus lower the specificity.

These results indicate the potential of our fiber-optic confocal endoscope (FOCE) which has a similar axial resolution (5-6μm) and images in near real time. The primary difference between the FOCE and the present system is the addition of the fiber optic imaging bundle which decreases signal throughput and introduces background noise from reflections of the fiber faces. These constraints are being overcome using index matching oils to remove the specular reflection and increase throughput; we have recently obtained *in-vivo* images of the oral cavity using the FOCM with sufficient contrast to visualize subcellular detail [9].

The performance of the present system is comparable to *in-vivo* video rate confocal images taken with a system used to image the oral mucosa [1] and human skin [2]. The axial and lateral resolution of the present system (0.8 um lateral and 3-4 um axial) compare well with this system (0.5-1.0 um lateral and 3-5 um axial). The cell features in the images shown here are quite different than those of human skin [3] in which contrast originates from increased back-scattering from melanin within the cytoplasm [2] resulting in a relatively dark nucleus. In the present images the contrast originates from an increased back-scattering from the nucleus due to the interaction of acetic acid and the nucleus

[4] Our images are similar to images taken by Anderson, et. al. of the oral mucosa [1] at superficial imaging depths, but different deeper within the epithelium where nuclei visualized within the oral mucosa are dark, similar to the human skin. The contrast provided by the acetic acid has three primary advantages. After its application, the increased backscattering is uniform on virtually all nuclei in the field of view; nuclei can be visualized in images taken down through to the bottom of the epithelium and the edge between the nucleus and cytoplasm is distinct. These three characteristics enable improved quantitative measurements throughout the epithelium.

The sensitivity and specificity of the system's quantitative feature measurements (100% and 91% respectively) compare well with the results of quantitative pathology (Poulin, unpublished data, 1995) in distinguishing between high grade dysplasia (CIN II/III) and low grade dysplasia or normal tissue. In quantitative pathology, measurements of cellular and nuclear morphometric and architectural features from histologic slides are used to attempt the diagnoses of pathology. Using a morphometric index calculated using multiple nuclear morphologic measurements of archived histology slides, Mac Auley's group obtained a sensitivity of 90% using a specificity of 90%. The higher resolution and contrast from the stains allow many more types of morphometric measurements than those made from the confocal images. The obvious advantage of the confocal system is its ability to image *in vivo*.

This ability to image *in vivo* suggests the system's use in the diagnostic clinic. The high specificity of the instrument suggests its use for facilitating physicians' decision on where to obtain colposcopic biopsies. Many unnecessary

biopsies are currently taken due to the relatively low specificity of colposcopy. The use of the instrument for guiding biopsy direction could result in greater convenience to the patient and lower costs in diagnostic procedures.

Another use of the instrument might be to aid in the study of progression and regression of precancers in chemoprevention trials by tracking biomarkers. For example, there are ongoing chemoprevention trials using retinoic acids, to reverse precancerous lesions in the oral cavity and prevent second primary tumors in patients who have successfully completed treatment for head and neck cancers [37]. Patients who have developed one head and neck cancer are very prone to a second primary, because the entire epithelial lining is at risk for neoplastic changes (field effect). In order to evaluate the effectiveness of these agents, multiple biopsies must be obtained over time to evaluate the tissue at risk. However, the biopsy process itself affects the field – small foci of pre-cancerous cells may be removed and the resulting repair process disrupts the field. Further, many patients hesitate to enroll in such trials because of the multiple biopsies. *In vivo* optical imaging modalities, such as confocal microscopy, which can visualize cells and nuclei throughout the epithelium and give information about nuclear size and texture features, may provide a tool to monitor the field at risk without the need for biopsy, providing a powerful new tool to aid in chemoprevention studies.

We are continuing our analysis of the images deeper into the tissue in order to differentiate between low-grade dysplasia and normal tissue, however the variation in penetration depth limits the number of biopsies that can be imaged near the basement membrane. A larger study would provide adequate sample numbers to study these lesions. We are also studying the effect that changes in the

scattering coefficient might have on the diagnostic sensitivity of the system. Future plans include *in vivo* imaging of the cervix with the FOCM. The present results indicate the clinical potential of *in vivo* confocal imaging.

Part 2 - Confocal System Improvements

4.2.1 INTRODUCTION

In order to acquire the necessary data for the studies described in Chapters 5 and 6, the confocal microscope was modified to acquire three dimensional image sets. Improvements in the system sensitivity were also made in order to potentially improve image penetration depth in abnormal tissue. The remainder of this chapter describes these modifications.

4.2.2 3D IMAGE ACQUISITION DESIGN

In order to acquire three dimensional image sets efficiently and accurately, the micrometer on the system must be replaced with an automated, actuated micrometer. The two primary features which must be considered in moving the sample stage in the axial direction is the image depth spacing and the movement of the actuator which could cause motion artifact. In order to prevent aliasing in the axial dimension the images should be maximally spaced at half the axial resolution of the system (3-4 μm). To prevent motion artifact, it would be preferable to move the sample, wait for the sample to settle and then acquire the next frame. Considering the possible number of images needed in a set (300 μm deep epithelium divided by 2 μm/image equals 150 images) and the time between images (up to 0.25 seconds) this procedure would take approximately 40 seconds to acquire an image set. Since the image sets must be stored in the computers RAM during acquisition, it would be preferable to speed up the acquisition time. Another disadvantage of this method is the requirement to synchronize the axial movement of the sample with the image acquisition timing.

An alternative procedure for acquiring image sets is to move the specimen stage through the image plane in one smooth motion and acquire images along the way. This introduces two potential problems, motion artifact and image plane distortion or image tilting caused by the sample movement between acquiring the top portion of the frame and the bottom portion (Figure 4.7). It turns out that these problems can be sufficiently minimized by moving the sample slow enough to meet the Nyquist sampling criteria in the depth dimension. To meet this criterion, the specimen stage must be moved no more than 2 μm between successive frames since the axial resolution is 4 μm. This limits the stage speed to 15 μm per second (2 μm per frame X 7.5 frames per second = 15 μm per second). The image tilt in this case is less than 2 μm. At this speed motion artifact is insignificant since the movement of the stage during the acquisition time of each pixel is less than a nanometer (1 μs per pixel X 15 μm per second = 15 picometers per pixel). Using a specimen stage speed of 15 μm per second, an image set can be acquired of a 300 μm epithelium in 20 seconds.

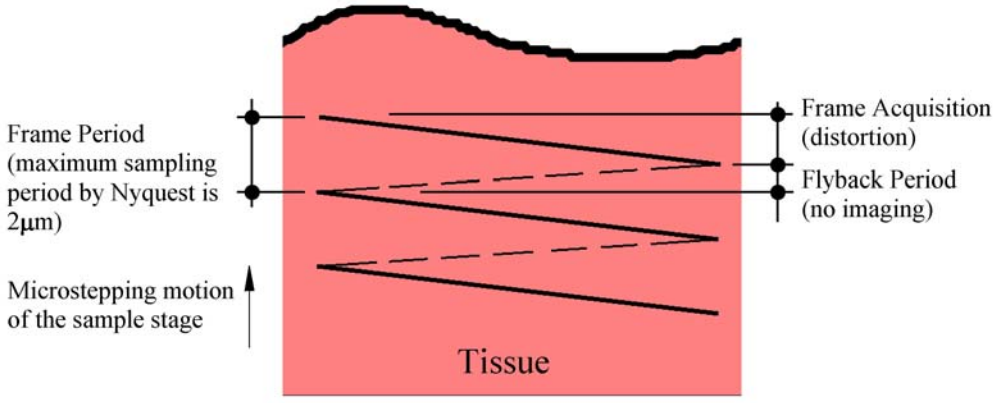

Figure 4.7 Sample stage movement during three dimensional image set acquisition.

The two options for actuators are stepper motor type and DC motor. The DC motor will not provide even motion at rates this slow, but stepper motors can. The potential drawback of using a stepper motor is that the discrete stepping motion itself could cause motion artifact, however most stepper motors can be micro stepped to create motion smooth enough to avoid large steps (comparable to the axial resolution). A CMA actuator driven by an ESP300 driver both by Newport can provide accurate and smooth movement at speeds this slow and was chosen for the subsequent work.

4.2.3 SENSITIVITY IMPROVEMENT DESIGN

In the images shown in Chapter 3 and the first part of this chapter, the image penetration depth appeared to be limited by the instrument and not by background scattering from sample. To improve the depth of image acquisition, either the laser source power must be increased or more of the signal leaving the tissue must be collected. Increasing background noise is a potential consequence of increasing the intensity of the source light at the tissue. However since increases in background noise with imaging depth have not been observed in the previous studies, it was not anticipated that moderate increases in the source light would cause significant background increase. To maintain the portability of the system and keep costs reduced, the current small diode laser source was not replaced. To acquire more signal from the tissue, two modifications were considered. 1). Replace the objective's immersion fluid with one with an index which is closer to the tissue index. This same method has been performed by Rajadhyaksha et al [1]. They replaced the water immersion fluid with a glucose

solution. This reduced the reflection off the tissue surface and has the added advantage of reducing the wave front distortion as the source and signal light pass the immersion fluid / tissue interface. The objective, which is currently on the system, is designed for use with immersion fluids of varying indexes. 2). Rotate the polarization of the signal light so that the beam splitter will transmit more light through the confocal system. On the system used for the previously described studies, 50% of the source light is lost at the beam splitter as the light propagates to the sample and 50% of the signal is lost as the signal light is reflected towards the detector. These losses can be reduced by using a polarization dependent beamsplitter with a preferential reflection at one polarization and a preferential transmission at the opposite polarization. Light propagating from the source to the sample can be transmitted preferentially toward the sample. The polarization of the light can then be rotated 90 degrees before it arrives back at the beam splitter. This signal light can then be preferentially reflected by the beamsplitter to the detector. The rotation of the polarization would be accomplished by placing a ¼ wave plate between the beam splitter and the sample such that the light reaching the sample is circularly polarized. Upon reflection, the light remains circularly polarized but in the opposite direction. After passing through the ¼ wave plate on the return trip, the light is polarized 90 degrees to the original light. Beam splitters up to 90/10 can be acquired. I chose an 80/20 beamsplitter due to availability. Due to the polarization and wavelength sensitivity of the chosen beamsplitter, the actual throughput of the 80/20 beamsplitter was 60 percent of the signal light transmitted toward the sample stage upon the first pass through the beam splitter, and 95% of

the signal light reflected towards the detector upon the return path. The theoretical throughput of the original 50/50 beamsplitter was $50\%^2$ or 25%. The theoretical throughput with the new configuration is 60% X 95% X 2(96%) = 52%, where the 96% is due to losses off the ¼ wave plate both to and from the sample stage. This results in a 2.1 improvement in throughput.

4.2.4 SYSTEM MODIFICATION RESULTS

After the modifications of the system, I tested the increase in signal by imaging a glass slide. The signal at the detector increased by a factor of 1.9 which compared reasonably well with the design value of 2.1.

The signal to noise was also measured both before and after the modifications. To make an appropriate measure of the signal to noise, it is necessary to measure the noise under the same conditions as tissue imaging. Unfortunately, estimating the noise from the tissue images is difficult since it is difficult to separate signal modulation due to noise from signal modulation due to microscopic tissue motion. Two methods were used to estimate the noise. First the modulation of the signal was measured from an area adjacent in X and Y to the tissue image, and second the noise was record from the detector with the focal plane of the objective several 100 μm above the tissue. These values were compared to the mean signal acquired from the tissue. Under carefully controlled conditions the signal to noise approached 20 both before and after the system modifications. Under more realistic (normal clinical operation) conditions the signal to noise was measured at approximately 17. The difference between the optimal and normal conditions is dependent on the X/Y position of the confocal

pinhole. Both the noise and signal level are dependant on minor changes in this position.

In order to improve the rejection of specular reflection off the tissue surface and reduce wave front distortion at the front surface of tissue, the performance of three immersion media were compared: PBS (used in the previously described studies), glucose and glycerol. The media were tested under two different conditions. The first test was performed as a part of a separate study which used the confocal system to image hamster check pouches *in vivo*. A minor reduction in the specular reflection from the tissue was observed with the glycerol. There was little measurable reduction in reflection from the tissue surface as compared to the PBS using a 10% glucose solution. The second test was performed as a part of the studies described in Chapters 5 and 6. In this case, the immersion media was placed on cervical biopsies. Due to the detached nature of the biopsies, the glycerol penetrated the biopsy appearing to severely dehydrate it. The glucose did not provide any noticeable decrease in reflection from the surface of the biopsy. The remaining biopsies in these studies were therefore imaged using PBS to avoid any possible reaction with the immersion media.

In order to test the acquisition of 3D image sets, an image of a cervical biopsy was made with the added automated micrometer described above. Figure 4.8a shows a sample image acquired from the resulting image set. This image is a portion of a transverse section extracted from the 3D image set acquired with the focal plane perpendicular to the tissue surface. Two things are apparent from the image. First, the resolution is reduced as compared to the typical en face images, Figure 4.8b. This is to be expected due to the 4-fold reduction in resolution in the

axial dimension of the confocal microscope. The other apparent features in the image are the visible nuclei. Since each nuclei is contiguous along the axial dimension, the acquisition of the 3D image set appears to be positionally stable as the sample stage is translated.

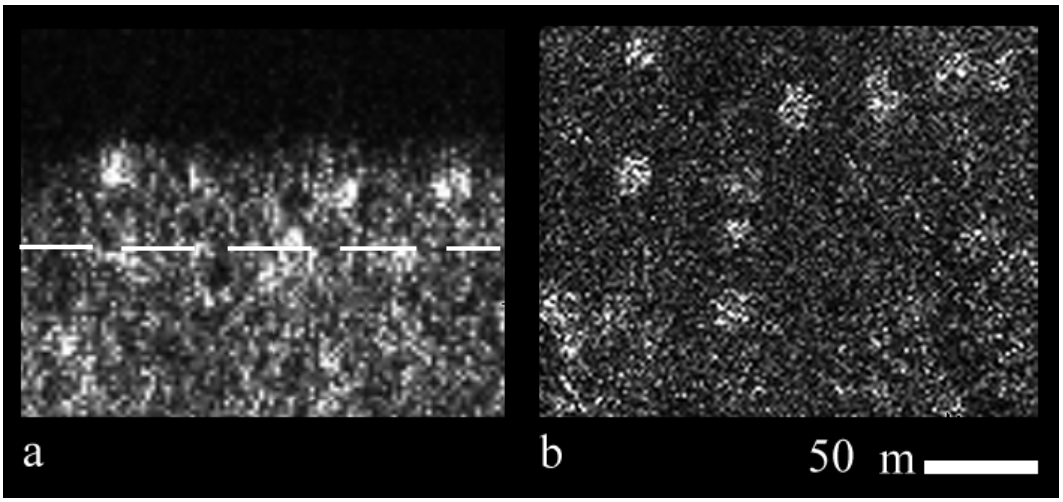

Figure 4.8. Comparison of a transverse image section (a) and *en face* image (b) taken from a 3D confocal image set. The dashed line in (a) indicates the location of the perpendicular section (b).

The reduced resolution in the axial dimension has important implications for the 3D quantitative feature extraction study described in Chapter 6. Although the added third dimension provides additional information, the information obtainable from the axial dimension is ¼ per unit of tissue as compared to the other two dimensions. Figure 4.8b shows a representative 2D image from which Figure 4.8a was composed. The difference in resolution is apparent.

CHAPTER 5

Sources of scattering in cervical tissue: determination of the scattering coefficient using confocal microscopy

5.1 INTRODUCTION

The interaction of light with tissue provides a noninvasive tool to monitor biochemical, morphologic and architectural changes associated with disease. A number of recent clinical trials have demonstrated the potential of real-time, quantitative optical spectroscopy and imaging technologies to aid in the early detection of disease [38-46]. Many of these techniques, including fluorescence and reflectance spectroscopy and imaging [38-44,49], Raman spectroscopy [50, 51], confocal imaging [27, 52,53] and optical coherence tomography (OCT) [54, 55] have demonstrated potential to detect early changes associated with the dysplasia to carcinoma sequence [56, 57], including increased nuclear size, pleomorphism and nuclear to cytoplasmic ratio, increased metabolic activity of epithelial cells, increased angiogenesis, and decreased structural protein density associated with precancer [58]. At the same time, more sophisticated models have recently been developed to aid in the analysis of optical signals and directly extract quantitative information about these biochemical and structural changes [59, 60, 61]. These models have been used to suggest new fiber optic probe geometries to maximize the contrast between optical signals of normal and precancerous tissue [59, 61, 62, 63, 64, 65].

Despite the promise of this approach, such models rely on accurate knowledge of the optical properties of the normal and precancerous epithelium and stroma in order to provide useful information to analyze tissue data and to guide the development of fiber optic probes for in vivo use. In particular, these models require accurate values for the absorption coefficient, the scattering coefficient and the scattering anisotropy of both the epithelium and the stroma.

Several methods have been developed to compute the optical properties of tissue from measurements of collimated transmission, diffuse transmission, and diffuse reflectance [66, 67, 68] or from reflectance measurements made at varying source detector separations [69, 70]. In general, these methods assume that the optical properties of the sample are homogeneous; recent work [60, 71] has shown that the optical properties vary throughout the epithelium, and that this variation is correlated with both clinical factors, such as the patient's age, and with disease-related factors, such as the presence or absence of precancer. While optical properties have been derived using approaches based on the assumption of homogeneity for a number of epithelial tissues, including the bladder, colon, skin and esophagus [66, 72, 73], it is likely that the reported values are dominated by the optical properties of the stroma, which occupies the largest volume fraction of the tissue and which likely has the largest absorption and scattering coefficients.

In order to use multi-layer models of tissue spectroscopy to analyze data acquired in vivo [74] and to design sophisticated fiber optic probes to separate signals from different epithelial and stromal layers [65], there is a critical need for accurate values for the optical properties of the epithelium, and to understand the

length scales over which they vary. In an attempt to address this need, Qu and colleagues microdissected the epithelium of bronchial tissue and separately measured scattering of the epithelium and stroma. They measured scattering coefficients of 200 and 225 cm^{-1} at 700 nm for epithelial and stromal tissue respectively [75]. Optical sectioning provides an alternative approach to physical sectioning; using reflectance based confocal microscopy, the depth dependence of reflected light from epithelial cells can easily be probed [27, 52, 53]. Several groups have measured the depth dependent decay of reflected light in tissue phantoms using both OCT and confocal microscopy; intensity was observed to decay exponentially according to the scattering coefficient [19,76, 77].

We previously [78] measured the depth dependent decay of reflected intensity from normal and precancerous *ex vivo* cervical tissue samples using a confocal microscope. We used these data to estimate the average epithelial scattering coefficient. In this analysis, we assumed that the reflectance intensity as a function of depth, I(z), could be expressed as:

$$I(z) = I_0 e^{-\mu_t z} \mathrm{R} e^{-\mu_t z} = I_0 \mathrm{R} e^{-2\mu_t z} \tag{5.1}$$

where I_o is the incident intensity, R is the average reflectivity, and μ_t is the attenuation coefficient, which is the sum of the absorption and scattering coefficients. Equation (1) assumes that excitation and reflected light travel parallel to the optical axis, which is equivalent to assuming a low numerical aperture. Further, it assumes that the tissue reflectivity and attenuation coefficients are independent of depth. Equation (1) was used to analyze

measurements of the intensity of reflected light measured as a function of depth to extract the average attenuation coefficient of the epithelium. In the near infrared, where confocal measurements are frequently made, the scattering coefficient is significantly greater than the absorption coefficient, so that this process was used to estimate the epithelial tissue scattering coefficient [75]. In this previous study, reflectance values were measured at a limited number of depths, so that the depth dependence of the attenuation coefficient could not be estimated. However, previously reported computational estimates of the tissue scattering coefficient indicate that the scattering coefficient of cervical tissue likely varies substantially throughout the epithelium [71]. The scattering cross section of normal cervical epithelial cells decreases as one goes from the superficial to the intermediate layer, but then increases in the basal/parabasal layer [71]. The scattering cross sections are significantly greater for dysplastic cells.

The goal of the present study is to measure confocal reflectance images of normal and precancerous cervical tissue at a greater number of depths throughout the epithelium. We analyze these data qualitatively to understand the variations in sources of image contrast throughout the epithelium. Furthermore, we analyze these data quantitatively to estimate the depth-dependence of the epithelial scattering coefficient in cervical tissue. In order to investigate the potential differences in scattering within different types of epithelium, measurements were made from normal cervical tissue as well as potentially precancerous regions.

5.2 METHOD AND MATERIALS

5.2.1 Patients

Cervical biopsies were acquired from twenty-eight patients at the Colposcopy Clinic at the University of Texas M.D. Anderson Cancer Center, in Houston, Texas. The patients were referred to the clinic for suspected dysplasia on the basis of an abnormal cervical cytology or for removal of cervical tissue using the loop electrical excision procedure (LEEP) due to a previous diagnosis of dysplasia. Informed consent was obtained from each patient, and the project was reviewed and approved by the Surveillance Committee at the University of Texas M.D. Anderson Cancer Center and the Institutional Review Board at the University of Texas at Austin.

5.2.2 Specimens

Four uterine cervix biopsies were acquired from each patient under colposcopic guidance. Two adjacent biopsies were taken from a colposcopically normal area and two adjacent biopsies were taken from a colposcopically abnormal area of the cervix. Biopsies were immediately placed in growth media (DMEM, no phenol red). Colposcopic impression (normal/abnormal) was recorded for each biopsy. The biopsies were approximately 3 mm wide by 4 mm long by 2 mm thick. One normal and abnormal biopsy pair were submitted for routine histologic examination using the hemotoxylin and eosin (H&E) stain. Sections were examined by an experienced, board certified gynecologic pathologist (AM). The other normal and abnormal biopsy pair were embedded in agarose and a portion of each biopsy was sectioned transversely into

approximately 200 μm thick sections using a Krumdieck tissue slicer. The fresh tissue sections and remaining biopsy, after removal from the agarose, were placed back in growth medium. Reflectance confocal images were obtained from the transverse tissue sections and the remaining intact portion of the biopsy within 2 hours of sectioning and within 4 hours of excision. Confocal images were obtained from the transverse fresh tissue slices with the focal plane of the microscope oriented parallel to the tissue slice, resulting in transverse images. Confocal images of the remaining intact portion of the biopsy were obtained with the focal plane of the microscope parallel to the epithelial tissue surface, resulting in en face images.

5.2.3 Confocal Imaging

Reflectance confocal images were obtained from each biopsy using an epi-illumination laser scanning confocal microscope described in [10], with minor modification. The illumination source was a continuous wave diode laser operating at 810 nm. Images were acquired with a 25X 0.8 NA water immersion objective (Plan-Neofluar multi-immersion, Zeiss). The confocal system operates at a dimensionless pinhole radius of 2.5. The measured lateral and axial resolution of the system are 0.8 microns and 2-3 microns respectively. The beamsplitter used in [10] was replaced with a polarizing beamsplitter in order to increase the transmission of the laser source and collection of signal light. A quarter wave plate was added between the beamsplitter and sample in order to rotate the polarization of the reflected signal light.

Immediately prior to imaging, biopsies and biopsy sections were removed from the growth medium and rinsed with PBS. Image frames were acquired at various epithelial depths in 1.5 μm intervals up to the 250 μm working distance of the microscope. Then, a 6% solution of acetic acid was then added to each sample, and the image sequence was repeated. Images were digitized using a video frame grabber card and displayed at 6.5 frames per second on a computer monitor. Individual bitmap image files were saved from the frame grabber's video buffer. Uncompressed video files were also acquired from the video buffer as each sample was moved toward the objective in order to acquire images at a depth spacing of 1.5 μm. The image depth was adjusted by moving the sample stage using a stepper motor; the translation rate was sufficiently slow as to avoid motion artifact and image distortion. The confocal images were also compared to the corresponding H&E stained images from the adjacent biopsies in order to compare the morphology visible in the confocal and histologic images.

5.2.4 Image Processing

Images from each biopsy were processed to extract the mean reflected intensity from the image, and from various features within each image, such as cell nuclei, as a function of depth beneath the tissue surface. At each image depth, the mean gray scale intensity was measured from each image. We used a segmentation algorithm to automatically segment cell nuclei within each image [79], and we extracted the mean reflectance intensity from all segmented nuclei as a function of depth. The segmentation algorithm is described in detail in [79]. Briefly, as a first processing step we employed a powerful non-linear edge-

preserving image filtering technique - anisotropic median-diffusion - to increase the signal-to-background ratio. Next, knowing that the images of the nuclei exhibit strong local dependencies, while exhibiting a wide range of gray scales, we utilized a Gaussian Markov random field (GMRF) to model these dependencies independent of the overall grayscale variations. Since objects other than nuclei are present in cervical tissue and our image model does not include non-nuclear objects, we reduced the number of non-nuclei by removing objects that are not present in successive frames and further reduced the number of non-nuclei using Bayesian classification. After segmentation, the mean reflected intensity of the nuclei and entire image were plotted as a function of depth from each biopsy.

5.3 RESULTS

Images were available from 27 biopsies from 16 patients; 17 of these were diagnosed as squamous normal tissue, 3 were diagnosed as high grade squamous intraepithelial lesions (HGSILs) and 7 were diagnosed as low grade squamous intraepithelial lesions (LGSILs). Fresh tissue sectioning of 5 biopsies from 5 of these patients and 22 biopsies from the 12 other patients were not successful due to the small size or fragile nature of the biopsies. Images were not available from 2 biopsies from 2 patients.

Figure 5.1 shows the effect of acetic acid on the confocal reflectance images of the cervical epithelium and stroma. Brighter epithelial nuclei are visible in the epithelial images after the application of acetic acid. Fibroblast nuclei can also be seen in the fibrous tissue of the stroma after application of

acetic acid, although they are smaller and less uniformly distributed than epithelial nuclei.

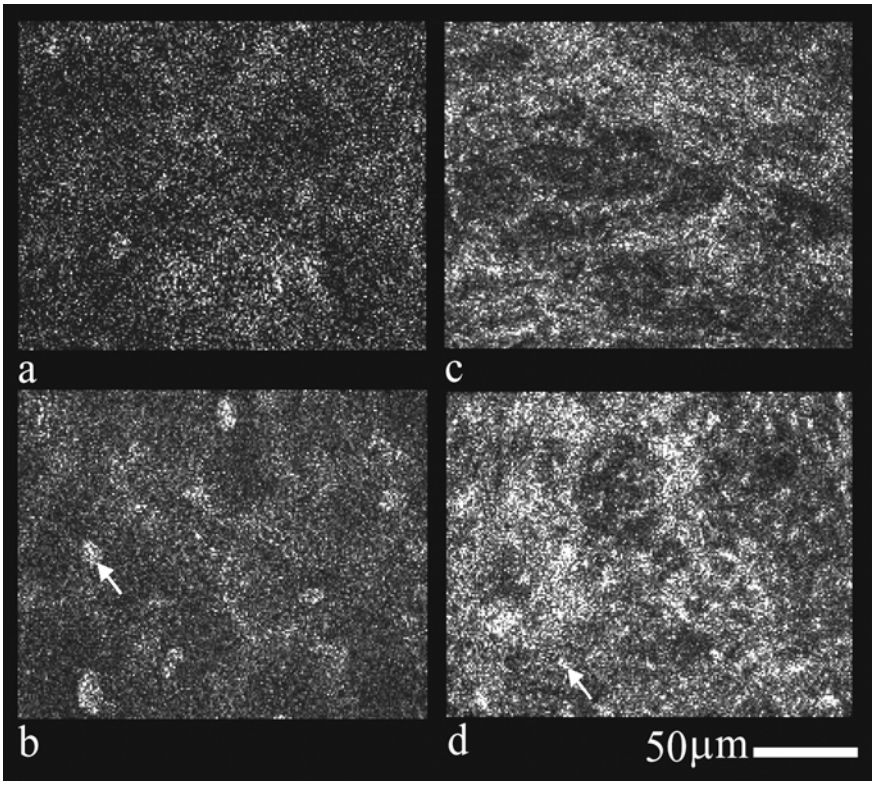

Figure 5.1. Confocal images of cervical epithelium (a, b) and stroma (c, d) before and after the application of acetic acid. Nuclei are barely visible in the images taken without acetic acid (a, c) but are significantly brighter (arrows) after the application of acetic acid (b, d).

We examined the confocal image stacks of the 27 biopsies obtained post-acetic acid, and observed that all the images could be grouped into several types of image patterns. Figure 5.2 shows representative images from these image patterns. In the superficial epithelium, approximately half the biopsies showed

images with a bright, speckled pattern of varying density as illustrated in Figs. 5.2a and 5.2b. This pattern is consistent with the location of keratin production in the upper epithelium. In most of these cases, the reflectance signal is localized to a relatively large area at the periphery of the cells and few nuclei are visible, as indicated by the arrow in Fig 5.2a. In 3 of the biopsies, this bright pattern covered most of the images and nuclei were difficult to distinguish from the speckled pattern (Fig. 5.2b). In the other half of the biopsies, the superficial and intermediate epithelium showed confocal images with little reflectance from the periphery of the cells and with bright reflectance from the cell nuclei; Fig. 5.2c shows an example of this type of image pattern. In biopsies with dysplasia, the superficial and intermediate epithelium showed a similar image pattern, except that the density of nuclei was much higher, as in Fig. 5.2d. The speckled pattern is also apparent at the periphery of cells in Figs 5.2c and 5.2d; however, is much less prominent and covers a much smaller area. Images of the basal epithelium also contained high-density nuclei, however the nuclei are smaller and much more dense (Fig 5.2e). Stromal images illustrate reflectance from collagen fibers and fibroblast nuclei (Fig. .2f). In many biopsies the transition between these regions was abrupt, and the image stacks reflected a 'layered' appearance within the epithelium.

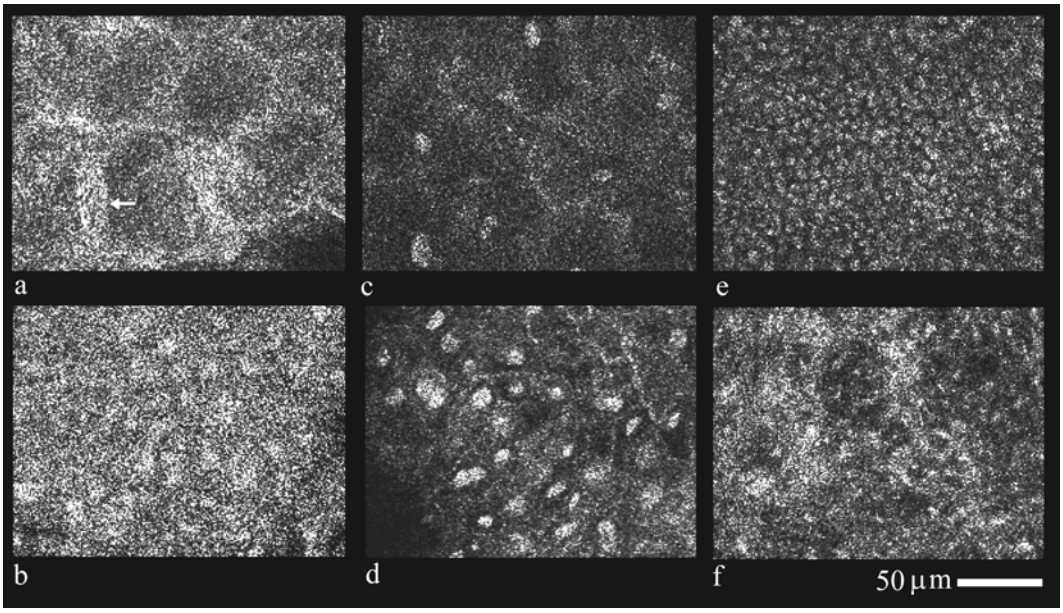

Figure 5.2. Confocal images of typical regions within the cervix. In the superficial epithelium a bright speckled pattern is found in approximately 50% of the images. The pattern is confined to the cell periphery in some superficial epithelium (a) but is found throughout the epithelium in others (b). An even, low density pattern of nuclei is associated with normal squamous cells in normal superficial epithelium (c), where as an irregular pattern of high density nuclei is associated with the presence of dysplasia (d). Near the basement membrane (e) cell nuclei are also dense but much smaller. In the stroma (f) collagen bundles are not easily resolved but produce a bright irregular pattern.

Table 5.1 shows the distribution of the different image patterns within the various regions of the cervix. Regions of low density nuclei are the dominant pattern observed in normal epithelium. The table also indicates the number of image sets with a mixture of the different images patterns and the number of image sets where insufficient signal was available for further analysis.

Distribution of Image Patterns				
	Tissue Layer			
Morphology	Superficial	Intermediate	Basal	Stroma
Keratin	0	0	0	0
Keratin with Nuclei	3	0	0	0
Low Density Nuclei	4	13	0	5
High Density Nuclei	3	4	6	0
Mixed Image Pattern	11	9	0	0
Insufficient Signal	0	1	21	0

Table 5.1. Distribution of image patterns from various depths within the cervix.

Figure 5.3 shows a comparison between the confocal images taken from the regions characterized in Table 5.1, comparing them with H&E stained histologic sections of the corresponding biopsies. In this figure, the confocal images are oriented parallel to the epithelial surface, while the histologic images are oriented perpendicular to the epithelial surface. The differences in nuclear density from the various regions correlate well between the confocal and histologic images (Fig. 5.3a-5.3f). The pattern of collagen bundles is also generally similar (Fig. 5.3g-5.3h). The bright speckled pattern in the confocal images of the superficial epithelium correlates well with a thickening of the stained area at the cell periphery (Fig. 5.3c-5.3f), suggesting that the speckled reflectance likely originates from scattering from keratin near the cell membrane.

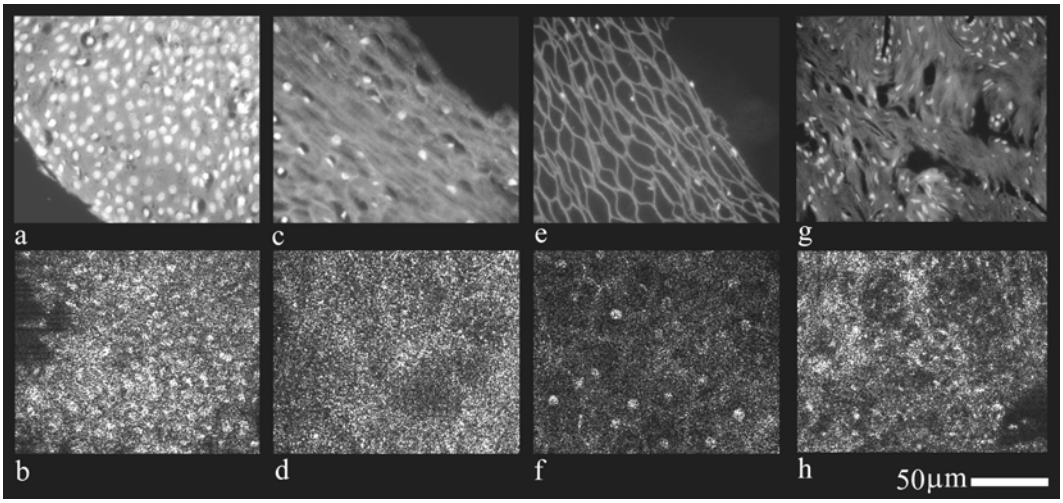

Figure 5.3. Comparison of *en face* confocal images (b, d, f, h) and transverse sectioned H&E stained images (a, c, e, g). Changes in nuclear density are consistent between the confocal (b, f) and H&E stained sections (a, e). The prominence of a bright speckled pattern in the confocal images (d, f) appears proportional to a thickening of the cell perimeter in the H&E stained sections (c, e). Confocal images (h) and H&E stained sections (g) of stromal tissue both show the prominence of the collagen matrix. All histologic images are shown as black and white images with the gray scale inverted.

Analysis of confocal reflectance images from the transverse fresh tissue indicated that the strength of the reflectance signal from nuclei did not vary appreciably within each region of the cervix, the superficial, intermediate or basal epithelium. Therefore, we analyzed the confocal image stacks to extract tissue scattering coefficient assuming that the strength of the reflectance, R, in Eq. (5.1) was constant within each region, independent of depth. However, we observed that the qualitative image morphology was homogeneous within distinct tissue layers, but then abruptly changed pattern. Thus, we applied, Eq. (5.1) to estimate the scattering coefficient within these homogeneous regions. Those regions noted as containing a mixed image pattern in Table 5.1 were therefore excluded from

this analysis. Twelve regions of interest were sorted into the categories of Table 1, based on their qualitative appearance. In the superficial and intermediate epithelium, these included regions of: (1) low nuclear density, (2) high nuclear density (3) keratinizing region with few visible nuclei and (4) keratinizing region with visible nuclei. Beneath the intermediate epithelium, these included regions of: (5) high nuclear density in the basal region, and (6) stroma. We analyzed images from each of the 6 categories obtained pre- and post-acetic acid. The image sets for the stromal data were taken from confocal images of the transverse tissue slices. In the stroma,, we again assumed that the reflectivity and tissue morphology were not depth dependent.

Figure 5.4 shows a typical plot of the average intensity of reflectance from nuclei as a function of depth beneath the epithelial surface; this graph also shows the mean reflectance intensity from the whole image. Corresponding images at several depths are shown at the top of the figure. Three distinct regions are apparent in Fig. 5.4: (1) first, a keratinizing region at the surface of the biopsy with bright nuclei, (2) second, a region of low-density nuclei in the superficial and intermediate epithelium (10-90 μm image depth), and (3) a region of high-density nuclei near the basement membrane (130-160 μm image depth). An increase in the signal is apparent near 120 μm; the rise in the mean image intensity is due to the increased nuclear density near the basement membrane. Figure 5.5 shows another plot on a log scale, which clearly indicates regions of the sample where the signal decays at different rates. We initially fit these data to Eq. (5.1) to extract the decay rates, with the expectation that both the mean reflectance from

the entire image and the mean reflectance of the nuclei would decay at the same rate. However, unexpectedly, the exponential decay constants extracted from the depth dependent intensity of average nuclear reflectance and average image intensity were not the same in each image. Further image analysis revealed that each image contained a constant background signal, which we attribute to multiply scattered light generated outside the focal volume, but not completely rejected by the confocal pinhole. The magnitude of this background light was assessed from areas of the image which did not include nuclei or signal from the cell periphery, and was found to be between 10-20 gray levels depending on the biopsy but independent of the depth of the focal plane beneath the epithelial surface. We therefore fit the data to a modified form of Eq. (5.1):

$$I(z) = I_0 e^{-2\mu_t z} R + BG \tag{5.2}$$

where BG represents this multiply scattered background light.

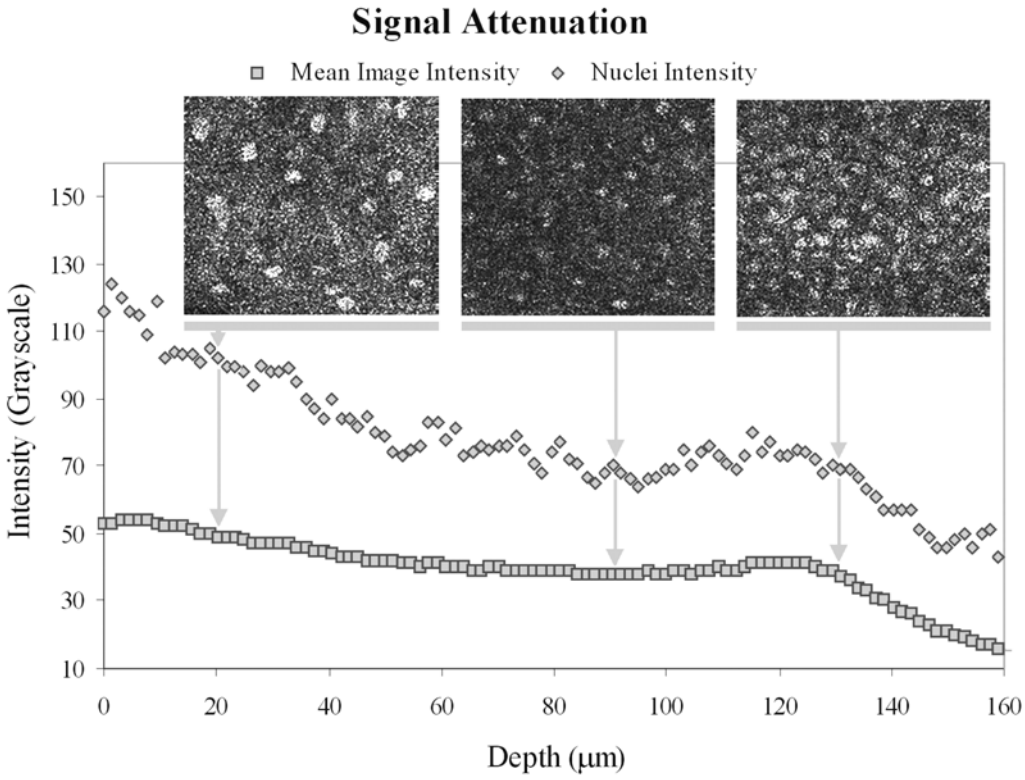

Figure 5.4. Typical confocal signal attenuation as a function of depth within a cervical biopsy. Both the mean nuclear intensity and mean image intensity show similar functional form with an exponential decay in two regions: the superficial layer (10-90 μm) and near the basement membrane (130-160 μm). Sample images used to acquire the data are shown at their respective depths (a-c).

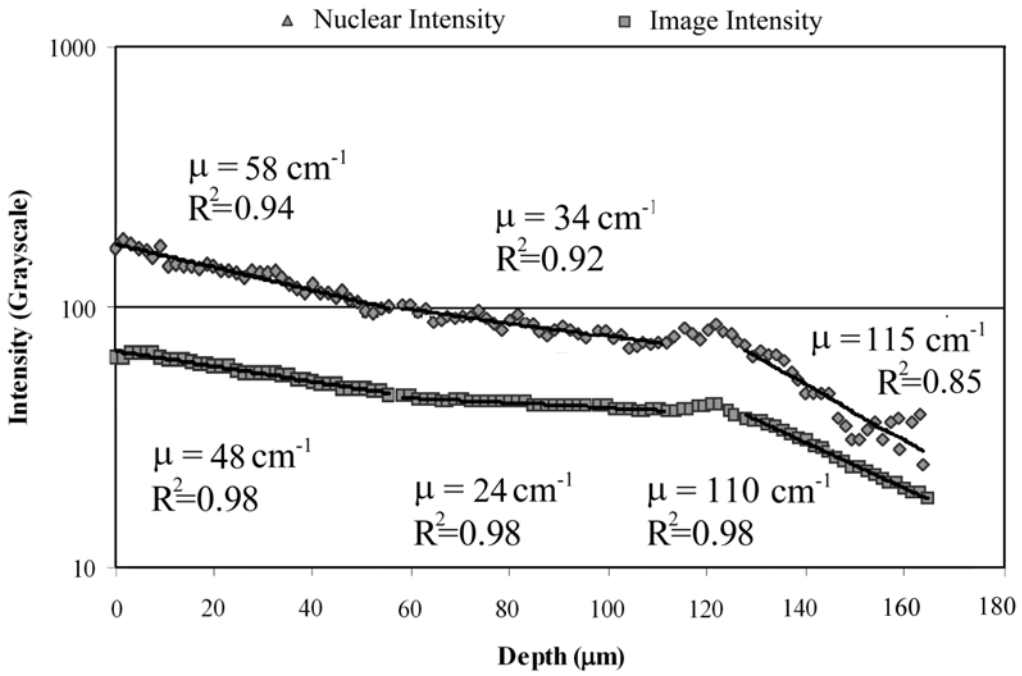

Figure 5.5. Exponential fits to the nuclear and mean image reflectance data for three regions of a sample biopsy.

The depth dependent intensity values of the mean nuclear reflectance and the mean image reflectance from 26 regions of 15 biopsies from 14 patients were fit to Eq. (5.1). Both the mean nuclear reflectance data and the mean reflectance data were simultaneously fit to Eq. (5.1) in the least squares sense; free parameters of the fit included R, BG and the attenuation coefficient. Fits were performed on data acquired both before and after application of acetic acid. Figure 5.6 shows the average values of the scattering coefficients extracted from these regions after the application of acetic acid. The scattering coefficients extracted from the superficial epithelium indicate that scattering is highest in regions where the reflectance from the cell periphery is strong. The average

regions where the reflectance from the cell periphery is strong. The average scattering coefficient drops in regions with low nuclear density, and increases as nuclear density increases near the basement membrane or in dysplasia. Beneath the basal epithelium, in the superficial stroma, the scattering coefficient increases. Interestingly, the scattering coefficients extracted from the image sets

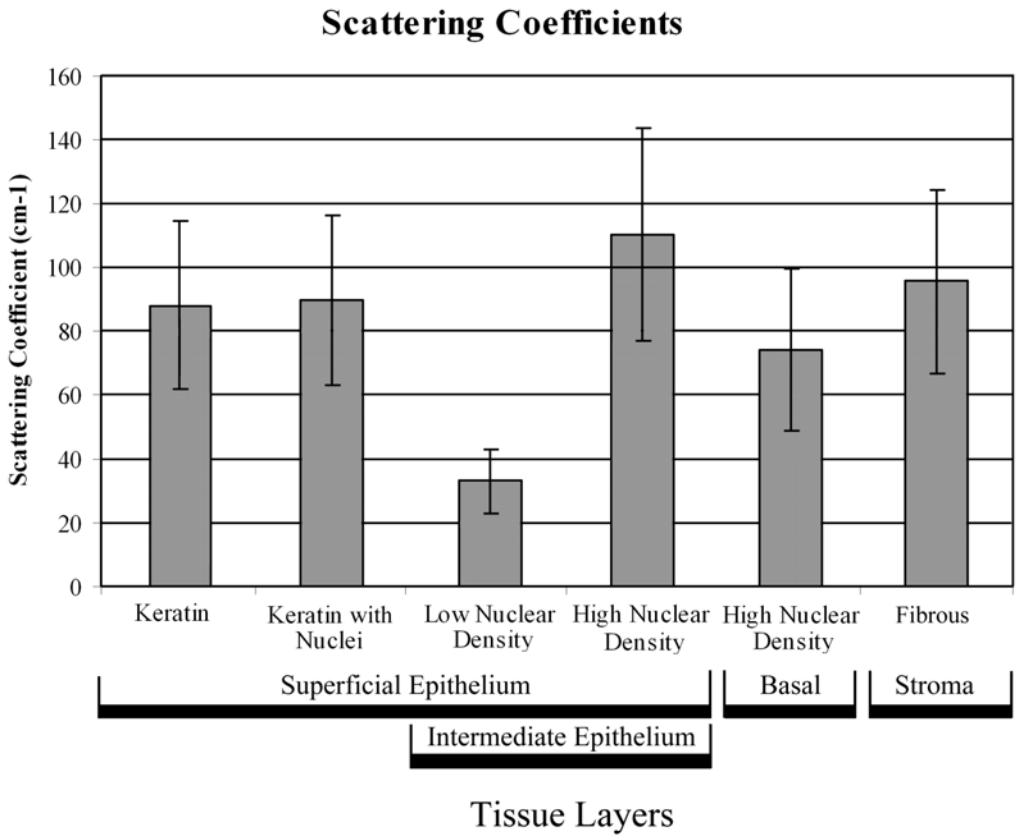

Figure 5.6. Scattering coefficients extracted from the various regions of the cervical biopsies. In the superficial and intermediate epithelium the scattering coefficient is governed largely by the presence or absence of keratin or high-density nuclei. Scattering values are consistently higher in the basal and stromal regions of the biopsies.

obtained before the application of acetic acid (data not shown) were not significantly different for areas with keratin or stroma, but were slightly lower for areas with low and high nuclear density

5.4 DISCUSSION

These results suggest that the two primary sources of scattering in the cervical epithelium are cell nuclei and keratin. Areas of epithelium with high nuclear density and/or keratin resulted in scattering coefficients that were 3 times higher than those for epithelial tissue with low nuclear density and little keratin. Areas with high nuclear density resulted in scattering coefficients which were a factor of 2-3 times greater than that associated with areas of low nuclear density. In normal tissue, high-density nuclei were associated with the basal layer of the epithelium, whereas in precancerous tissue, high nuclear density is associated with the presence of dysplasia, similar to our previously reported results [77]. The keratinizing regions were observed in the superficial epithelium in approximately half of the biopsies measured. In two-thirds of these biopsies the presence, and relative thickness, of this bright superficial layer prevented the resolution of subcellular detail in the basal layer. In most of the biopsies examined here, the scattering coefficient changed dramatically at a particular depth within the epithelium, and in no instance was the scattering coefficient homogeneous throughout the entire epithelium. Eighty percent of the normal biopsies contained the lower scattering region in either the superficial and/or intermediate epithelium. In approximately half of these normal biopsies the lower

scattering region was localized in the intermediate epithelium between a highly scattering superficial layer and highly scattering basal and stromal regions.

Table 5.2 compares the scattering values reported here with previously published results. Mourant[80] has previously studied the relationship between the wavelength and scattering and determined the scattering decreased as $1/\lambda^{1.1}$. This relationship has been used to calculate the values for other tissues in Table 2. The results presented here are slightly higher but not significantly different from the results we previously reported [78] which measured average scattering coefficients of 69 cm^{-1} for precancerous tissue and 22 cm^{-1} for normal tissue. We suspect the lower values to be a result of including the background, multiply scattered light in the analysis of this data. The value reported here for low-density nuclear tissue (33 cm^{-1}), which predominate in the intermediate epithelium, is also lower than values previously reported in bulk tissue scattering measurements for cervical tissue, 66-150 cm^{-1}. The high stromal scattering values suggest an explanation for this disparity. The significantly greater volume of stromal tissue compared to epithelial tissue reduces the contribution of the epithelium to the bulk tissue scattering values. The stromal values reported here are lower, but not significantly different than, values previously reported for RAFT cultures composed of rat tail collagen matrix and human fibroblast cells [81][50], 137 cm^{-1}. Based on qualitative observation of our images and images of cervical epithelium in [78], we suspect that the scattering values deep within the stroma are higher than the values reported here for superficial stroma. A limitation of the present study is the small number of patients and corresponding

limited number of homogeneous regions available for exponential fitting. A study of larger numbers of patients may better reveal common patterns of layered scattering within cervical tissue.

Reported Scattering Coefficients

Organ Site	Reference	Wavelength Measured (nm)	μ_s (cm^{-1})	μ_s (cm^{-1}) @ 810 nm
Keratinizing Cervix	This Paper	810	88	88
Cervix (Low Density Nuclei)	This Paper	810	33	33
Cervix (High Density Nuclei)	This Paper	810	110	110
Cervix Basal Layer	This Paper	810	75	75
Cervical Stroma	This Paper	810	96	96
Cervix (normal)	78	810	22	22
Cervix (precancerous)	78	810	69	69
Cervix	73	800	66-100	65-99
Uterus	66	635	394	301
Breast	82	810	150	150
Breast	83	1100	100-500	140-700
Bronchial tissue epithelium	75	700	200	170
Esophagus	72	630	70	53
Skin	66	633	187	143
Skin	84	810	370	370
Skin	85	1000	160	127

Table 5.2. Reported scattering coefficients from various tissue types [82, 83, 84, 85].

The results reported here have important implications for computational tissue modeling of epithelial tissue fluorescence and reflectance, and for optical probe design for *in vivo* data and image acquisition. The disparity in scattering between regions of the epithelium suggest that models which assume homogeneous scattering may not be well suited for predicting the propagation of

light through most cervical tissue. Based upon the scattering results, a homogeneous model might be valid for high grade dysplasia where high density nuclei are present throughout the epithelium. However, in normal tissue, two other scenarios appear to be possible. In the first the epithelium consists of two layers – a superficial and intermediate region containing low density nuclei, atop a basal layer containing high density nuclei – atop a highly scattering stroma. In the second, the epithelium consists, of three layers – a superficial, highly scattering keratinized layer, over an intermediate region of low density nuclei, with a basal layer of high-density nuclei underneath – atop a highly scattering stromal layer. The results also have important implications for the penetration of light into tissue. The presence of the low scattering regions in most biopsies implies deeper penetration of light into the tissue in most normal epithelial tissue.

Many computational models used to aid in the design of fiber based probes assume that the epithelium and stroma can be satisfactorily represented using a homogeneous scattering coefficient. Pfefer [63], Pogue [64] and Ramanujam [65] have shown that parameters such as the fiber diameter, source-to-collection fiber separation and probe-to-tissue surface distance all affect the mean path length and collection efficiency of optical probes and imaging systems. Pfefer presented an extensive Monte Carlo modeling study to investigate design parameters of the fiber optic probes. He studied the impact of tissue optical properties on fluorescence spectra assuming homogeneous optical properties with scattering coefficients ranging from 70-140 cm^{-1}. He found an increase in axial selectivity with decreasing fiber radius. Pogue demonstrated a fiber optic probe

where the signal intensity is not significantly affected by the medium's absorption and scattering coefficients, but depends only on the properties of the fluorophores. This design was based on Monte Carlo simulations of a homogeneous medium with a scattering coefficient of 100 cm^{-1}, well above what we find for the epithelial layer of cervical tissue. Ramanujam presented a concept to locate the depth of a target layer of precancerous tissue between a normal epithelial layer and a stromal layer. This method was based on exciting and recording the fluorescence through apertures of variable diameter. Assuming the same scattering coefficient for all three layers (100 cm^{-1}), she showed that the variable aperture imaging method could be used to determine the depth dependence of the fluorescence contrast provided by the precancerous epithelium. Again, these calculations assume a much larger epithelial scattering coefficient than measured here. The conclusions of all of these studies may not be applicable to the cervix and further study of probe design is needed for commonly encountered patterns of layered scattering.

Finally, the lower scattering values in the superficial and intermediate epithelium also suggest improved imaging depths for many imaging modalities. The fundamental limit for reflectance based imaging within tissue is high scattering. A change in the scattering coefficient from 100 cm^{-1} (the often assumed value) to 33 cm^{-1} results in an almost two fold increase in imaging depth for epi-illumination imaging. This is particularly significant for imaging modalities such as confocal and two-photon microscopy that use longer wavelengths where scattering of light within tissue is the most significant source

of signal loss. The presence of the highly scattering superficial layer has a detrimental impact on image penetration depth. Its occurrence in half of the biopsies for both normal and precancerous tissue implies that the image penetration depth is significantly dependent on patient-to-patient variability in keratin production.

CHAPTER 6

Comparison of 2D and 3D Near Real Time Confocal Microscopy for the Detection of Dysplasia

6.1 INTRODUCTION

Due to increased sampling, three dimensional imaging of cervical tissue has the potential to improve the detection of dysplastic tissue as compared to the two dimensional results reported in Chapter 4. The possible improvement is limited by the lower resolution of the third dimension in confocal microscopy; however it's ability to measure changes in cell differentiation throughout the epithelium is likely an important tool. The goal of this study is to evaluate the diagnostic potential of two and three-dimensional quantitative measurements extracted from confocal images, relative to standard pathology readings of normal and dysplastic cervical tissue. A comparison of the 2D and 3D features is performed to evaluate the benefits, if any, of acquiring the significantly larger amount of data required for 3D imaging. Both morphometric and architectural measurements extracted from 2D and 3D images are compared in the analysis. We find that improved separation between normal and CIN 2/3 biopsies can be obtained using 3D quantitative features as compared to similar 2D features. However with the addition of depth and scattering information, the 2D features are able to separate normal from CIN 2/3 comparably to 3D features based upon comparable p values.

6.2 MATERIALS AND METHODS

6.2.1. Patients

Cervical biopsies were acquired from twenty-nine patients at the Colposcopy Clinic at the University of Texas M.D. Anderson Cancer Center, in Houston, Texas. These are the same patients noted in the study in Chapter 5 plus one additional patient. The patients were referred to the clinic for suspected dysplasia on the basis of an abnormal cervical cytology or for removal of cervical tissue using the loop electrical excision procedure (LEEP) due to a previous diagnosis of dysplasia. Informed consent was obtained from each patient, and the project was reviewed and approved by the Surveillance Committee at the University of Texas M.D. Anderson Cancer Center and the Institutional Review Board at the University of Texas at Austin.

6.2.2. Specimens and Confocal Imaging

The specimens were acquired and imaged in the exact same manner as described in Chapter 5. Briefly, four uterine cervix biopsies were acquired from each patient under colposcopic guidance. Two adjacent biopsies were taken from a colposcopically normal area and two adjacent biopsies were taken from a colposcopically abnormal area of the cervix. Colposcopic impression (normal/abnormal) was recorded for each biopsy. One normal and abnormal biopsy pair were submitted for routine histologic examination using the hemotoxylin and eosin (H&E) stain. Sections were examined by an experienced, board certified gynecologic pathologist (AM). Reflectance confocal images were obtained from other normal and abnormal pair within 4 hours of excision.

Image frames were acquired at increasing epithelial depth in 1.5 μm intervals up to the 250 μm working distance of the microscope. Then, a 6% solution of acetic acid was added to each sample, and the image sequence was repeated. Images were digitized using a video frame grabber card and displayed at 6.5 frames per second on a computer monitor. Individual bitmap image files were saved from the frame grabber's video buffer. Uncompressed video files were also acquired from the video buffer as each sample was moved toward the objective in order to acquire images at a depth spacing of 1.5 μm. The image depth was adjusted by moving the sample stage using a stepper motor; the translation rate was sufficiently slow as to avoid motion artifact and image distortion.

6.2.3. Qualitative Image Review

The confocal images were compared to the corresponding H&E stained images from the adjacent biopsies in order to compare the morphology visible in the confocal and histologic images. The results of this comparison are presented in Chapter 5. The 2D and 3D confocal images were reviewed by individuals untrained in the diagnosis of dysplasia to determine the diagnostic potential of visual image review. After a brief training showing sample 2D and 3D images of normal and dysplastic confocal images of cervical tissue, each individual reviewed the sets of images from each sample and was asked to provide a diagnosis of normal or precancer based on this review. One set of images included the 3D image stacks taken from each biopsy compiled into a video with the focus moving from the top of the epithelium toward the basement membrane. The other set of images was composed of single 2D images taken from the same

set of biopsies with the focus of the microscope at 50 μm below the tissue surface. Each set was reviewed separately, and the order of the biopsies in each set was randomized. The sensitivity and specificity compared to standard histopathology was calculated for each individual reviewer; these values were compared for the 2D and 3D image sets. A comparison was also made between those individuals who have had previous experience viewing images with the confocal system and those with no previous experience.

6.2.4. Image Processing

Images from each biopsy were processed to segment the cell nuclei at each image depth. The segmentation algorithm described in Chapter 5 was used to aide in the segmentation. One additional level of nuclear size filtering was used to improve the segmentation as judged by a qualitative comparison between the segmented images and the originals. This filter removed segmented nuclei which were larger or smaller than the mean nuclear size +/- v times the standard deviation at that image depth, where v is a parameter varied to improve the segmentation. The value of v was varied between 1 and 2 to remove false positives as judge by a qualitative review. As a final step, minor corrections in the segmentation were performed by hand at each image depth to remove false positive nuclei based on visual analysis of images as the gold standard. No correction of the nuclear shape was performed. It is important to note that the effect of the minor corrections on nuclear thickness in the axial dimension is likely limited by the confocal axial resolution as is also likely the case with the automated segmentation. After segmentation, 2D images taken at 50 microns below the tissue surface and the entire 3D image sets were processed to extract

several morphological and architectural features. To narrow the number of features to include in the study, only features, which had previously been shown to aid in distinguishing between normal and dysplastic tissue, were included [86, 27, 87]. The mean and standard deviation of the following morphological features were extracted: nuclear area (from 2D images), nuclear volume (from 3D image stacks), maximum nuclear diameter and nuclear elongation. For the 3D features the mean and standard deviation was calculated over the entire volume. Cells at the basement membrane and immediately above were not included in the feature measurements.

The mean and standard deviation of the following architectural features were extracted: cell density, area disorder, volume disorder, mean distance between each cell and its neighbors (mean separation) and the minimum distance between each cell and its nearest neighbor (minimum separation). The architectural analysis of the images was based upon the calculated Euclidian centroids of all detected nuclei from the segmentation algorithm. The neighborhood of each cell was determined by tessellation of the nuclear centroids using the algorithms in Matlab, version 6.1. All cells with common boundaries were considered neighbors.

The morphologic and architectural features extracted from biopsies diagnosed as histologically normal and CIN 2/3 were compared. A Student's t-test was used to test the hypothesis that the mean values of these parameters were different between normal and CIN 2/3. Combinations of morphologic features, architectural features and scattering coefficients (reported in Chapter 5) were analyzed to determine the diagnostic potential for discriminating CIN 2/3 from normal tissue.

6.3 RESULTS AND DISCUSSION

Fifty-eight biopsies were obtained from 29 patients participating in the study. Imaging and successful segmentation were performed on 9 biopsies; 5 of these were diagnosed as squamous normal tissue and 4 were diagnosed as CIN 2 or CIN 2/3 (cervical intraepithelial neoplasia 2 or 3). Tissue processing of 27 biopsies was not successful due to the small size or fragile nature of the biopsies. Images were not available from 2 biopsies. Due to poor nuclear contrast, segmentation was not successful on 16 biopsies. Lastly, 3 biopsies were excluded due to a diagnosis of focal dysplasia and one with a diagnosis of koilocytosis. For the biopsies with focal dysplasia, no meaningful correlation could be expected from these biopsies since the volume of dysplasia is significantly smaller than the volume imaged from each biopsy.

6.3.1 Morphologic features

Figures 6.1 through 6.6 show the mean values of each feature over the five normal and five CIN 2/3 biopsies. Each figure shows the 2D and corresponding 3D features side by side. Average values are shown +/- one standard deviation over the various biopsies and the p values from the t-tests are also indicated. Figures 6.1 and 6.2 show the mean values for the morphologic features. In all cases, separation of normal and CIN 2/3 biopsies is greater using the 3D features. Figure 6.1 shows the mean nuclear area (extracted from the 2D images) and the mean nuclear volume (extracted from the 3D images). The 3D volume feature shows greater separation, but neither feature produces a significant difference. Figure 6.2a shows the mean maximum nuclear diameter. Neither the 2D nor 3D features produce a significant separation between the normal and CIN 2/3

biopsies. One notable feature of the plot is the marked reduction in the standard deviation of the 3D feature from the normal biopsies. Figure 6.2b plots this standard deviation as a separate feature. In this case the separation in the 3D feature is quite significant, and is the most successful single feature I measured for separating the normal from CIN 2/3 biopsies, p=0.003. Of the morphologic features, the nuclear elongation feature (data not shown) produced the smallest separation between the normal and CIN 2/3 biopsies

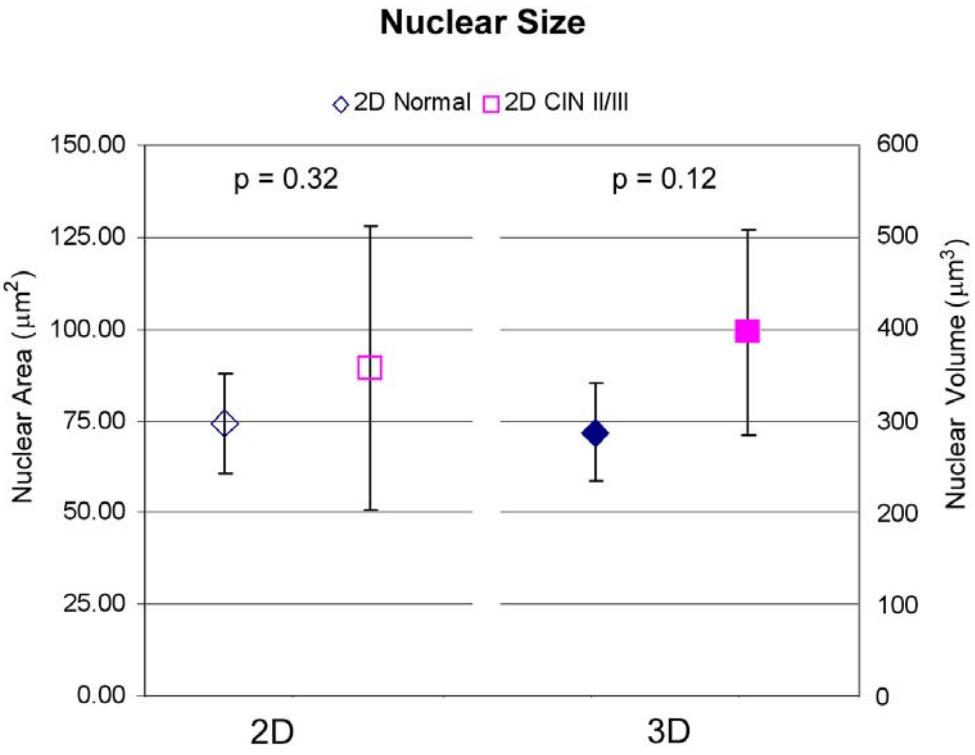

Figure 6.1. Comparison of the mean 2D and 3D nuclear size feature.

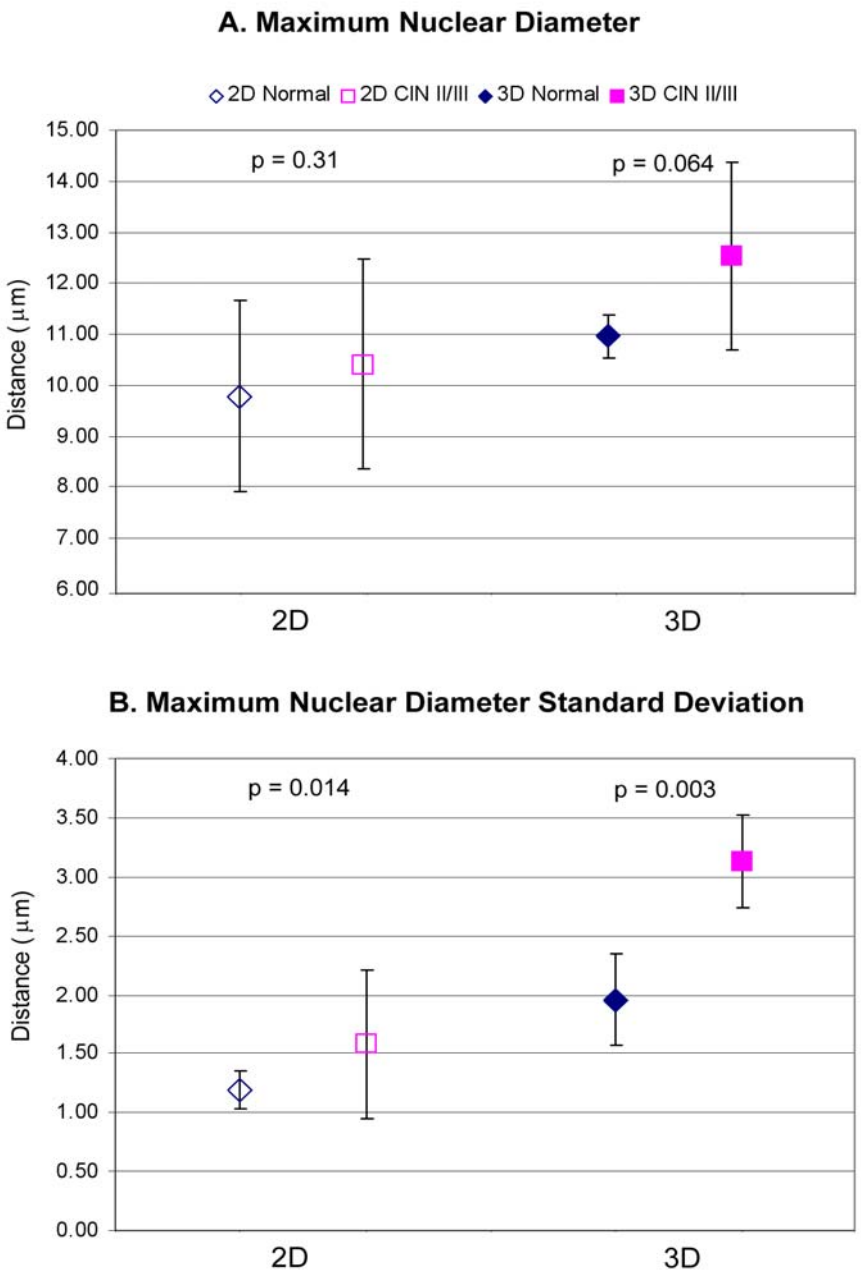

Figure 6.2. Comparison of the mean 2D and 3D values for two morphologic features: a) the maximum nuclear diameter and b) the standard deviation of the maximum nuclear diameter.

6.3.2 Architectural features

Figures 6.3-6.5 display the means and standard deviations of the architectural features. Again, in all cases except one, the 3D features perform better than the 2D features due to a smaller relative standard deviation in the 3D features. Figure 6.3 shows the difference in the mean cell separation features. The mean cell separation is greater in normal tissue than in CIN 2/3 biopsies in all cases. The standard deviation of this parameter was greatly reduced in the 3D analysis compared to the 2D analysis. This is partially due to a natural scaling of the standard deviation with the mean. However the large variation associated with the 2D cell separation is also partially due to the fact that all the 2D images are taken 50 μm below the surface, but the distance to the basement membrane varies between these normal biopsies. To account for this variation, I scaled the cell separations by dividing the mean cell separation by the ratio of the 50 μm acquisition depth to the total epithelial thickness. The epithelial thickness was measured by subtracting the image depth at which the tissue surface and basement membrane were encountered. For biopsies where the basement membrane could not be visualized, the thickness was measured from the images of the transverse tissue slices used in the study in Chapter 5. With this scaling, the standard deviation of the cell separation in normal biopsies is substantially reduced. This scaled separation data is presented in Figure 6.3 as the 2D + Depth feature. This reduction in the standard deviation improves the statistical significance for this 2D feature, with the p-value decreasing from 0.035 to 0.004. The p-value for the scaled 2D parameter is also less than that for the 3D version of this feature.

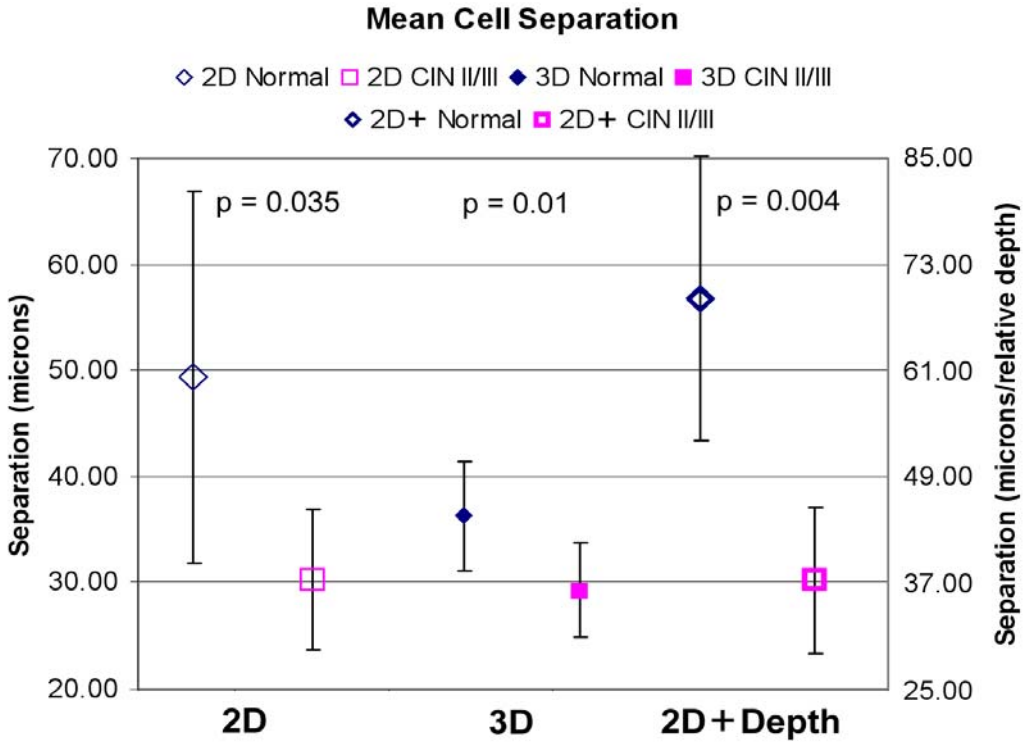

Figure 6.3. Comparison of the mean 2D, 3D and 2D + depth cell separation features.

Figure 6.4a shows the average values of the minimum cell separation feature extracted from the 2D, 2D + Depth and 3D images. The mean value of the minimum cell separation is greater in the normal images than in the images of samples with CIN 2/3. Again, the standard deviation associated with this parameter is substantially higher when extracted from 2D images than from 3D images, resulting in a reduction of the p-value from 0.039 in 2D to 0.012 in 3D. Figure 6.4b shows the standard deviation of the minimum cell separation as a separate feature. In this case, the 2D data show improved separation between the normal and CIN 2/3 biopsies. The 2D feature classification can again be improved by considering the ratio of the depth at which the image was acquired to

the epithelial thickness. The 2D + Depth again produces a greater separation than the 2D or 3D feature in both cases.

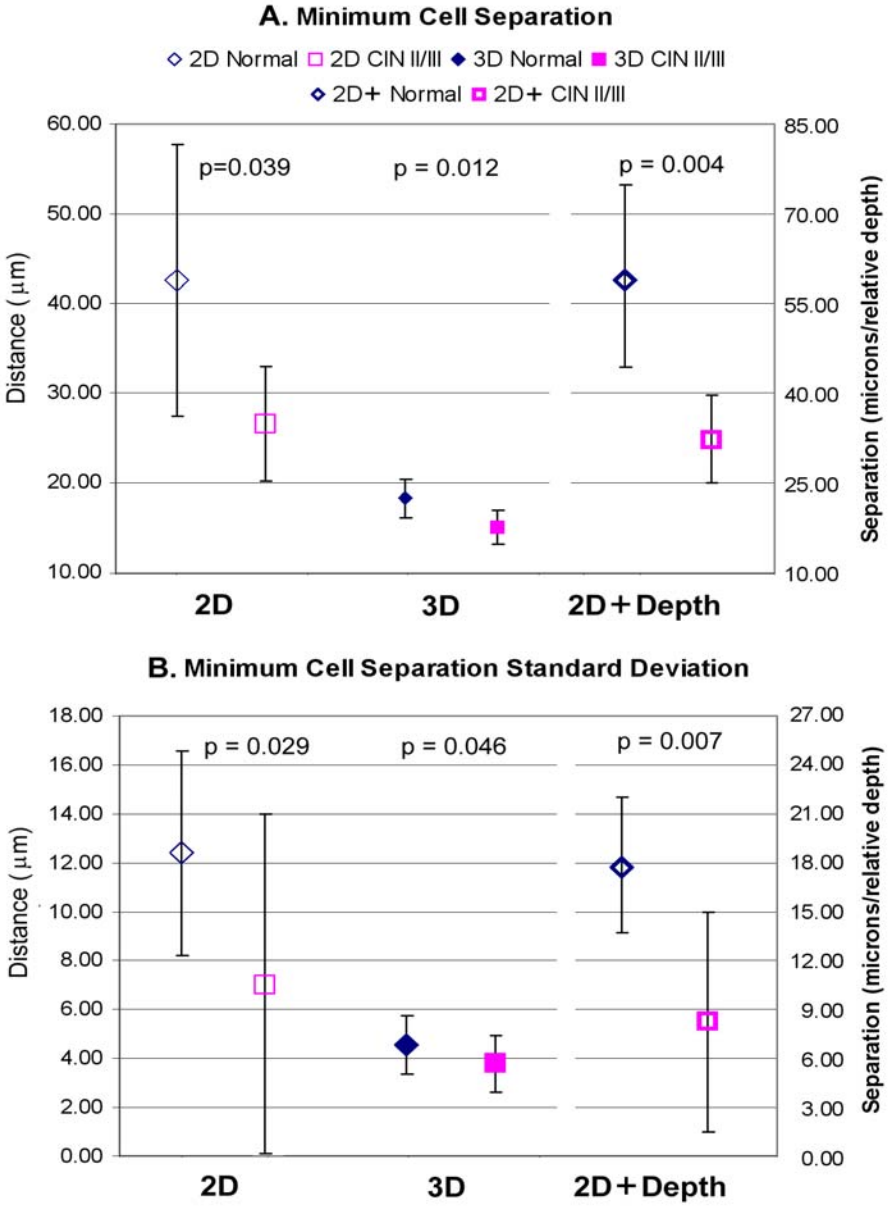

Figure 6.4 Comparison of the mean 2D and 3D values for two architectural features: a) the minimum cell separation and b). the standard deviation of the minimum cell separation.

Figure 6.5 shows the mean values for the cell density feature, the number of nuclei per unit area (2D) or per unit volume (3D). The mean density is increased in precancerous tissue, both in 2D and 3D. The 3D feature show statistically significant differences between normal and CIN II/III biopsies (p = .04) compared to the 2D features (p = 0.09).

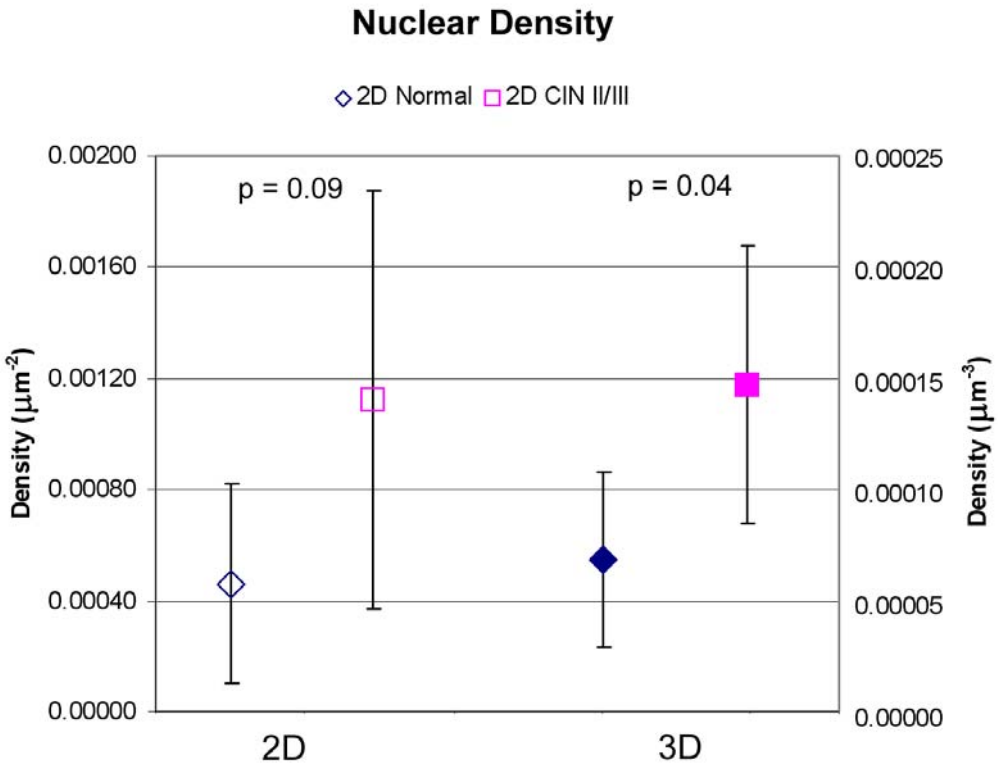

Figure 6.5. Comparison of the 2D and 3D nuclear density feature.

6.3.3 Feature Combinations

The combination of morphologic and architectural features produced improvements in separation between normal and CIN 2/3 samples, particularly in the 2D features. As expected, the best results were combinations which included the best performing morphologic feature (maximum nuclear diameter standard deviation) and the best performing architectural features (minimum and mean cell separation). Figure 6.6a shows the ratio of the mean cell separation to the maximum nuclear diameter standard deviation. The combination of greater cell separation and uniform nuclear size increase the feature values in the normal images as compared to the CIN 2/3. In this feature combination the 2D and 3D features produce a significant separation with improved performance in the 3D feature. Figure 6.6b shows the mean nuclear-to-cytoplasmic ratios over the normal and CIN II/III biopsies. The relatively smaller mean in the 3D parameter is due to a flattening of the nuclei in the depth dimension as is commonly seen in transverse sections of H&E stained slides. In this case only the 3D feature produces a significant separation between the normal and CIN 2/3 biopsies.

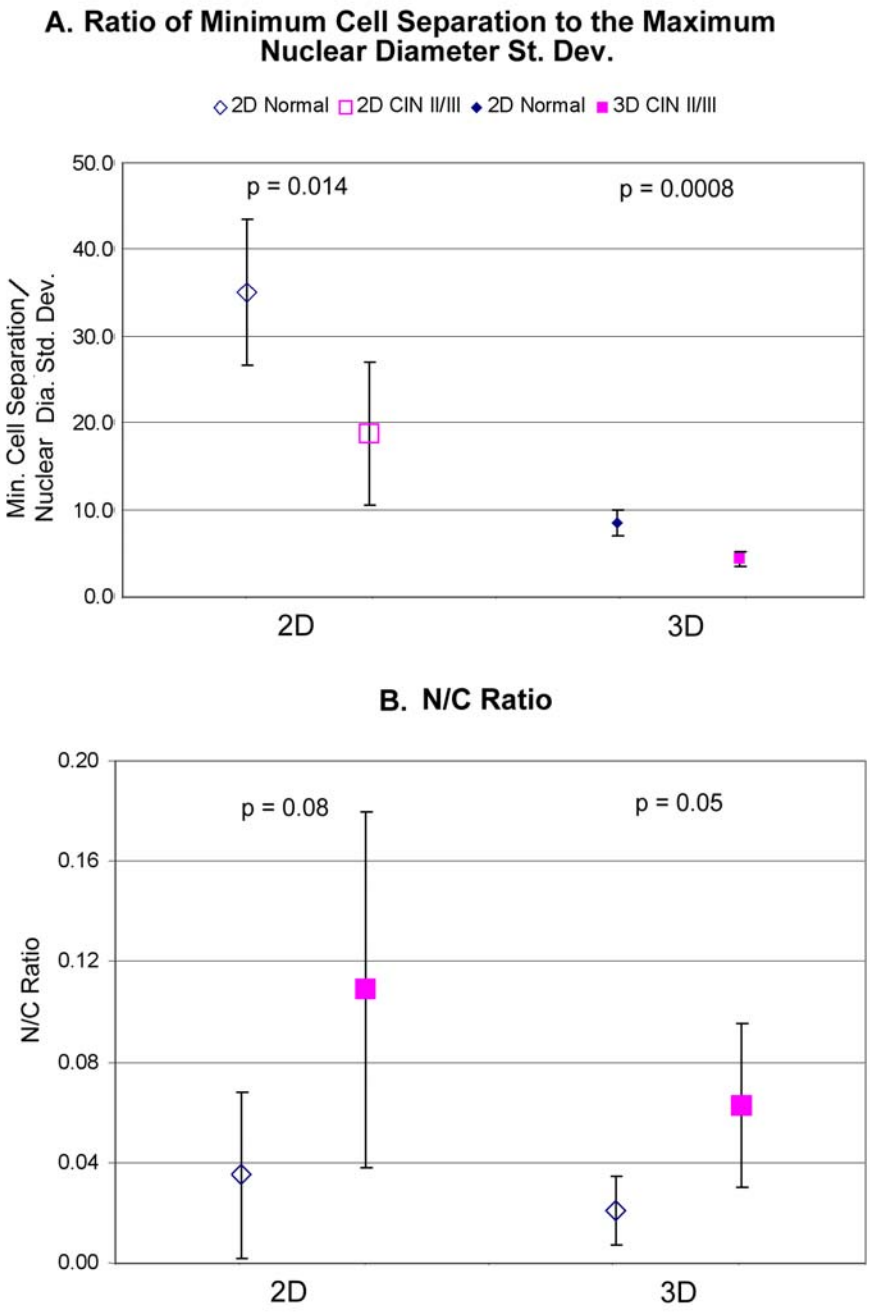

Figure 6.6 Comparison of the mean 2D and 3D values for two combination features: a) the ratio of minimum cell separation to maximum nuclear diameter standard deviation and b). the N/C ratio.

When the extracted scattering coefficient is combined with the morphologic and architectural features, a significant improvement is noted in the performance of the 2D features. Figure 6.7 shows the ratio of mean cell separation to the maximum nuclear diameter standard deviation for the 2D images and the same feature divided by the scattering coefficient. The scattering coefficient alone is also shown. The addition of the scattering coefficient reduces the p-value as compared to the 2D and scattering feature considered separately. The improved separation are similar to that produced by adding the epithelial thickness information.

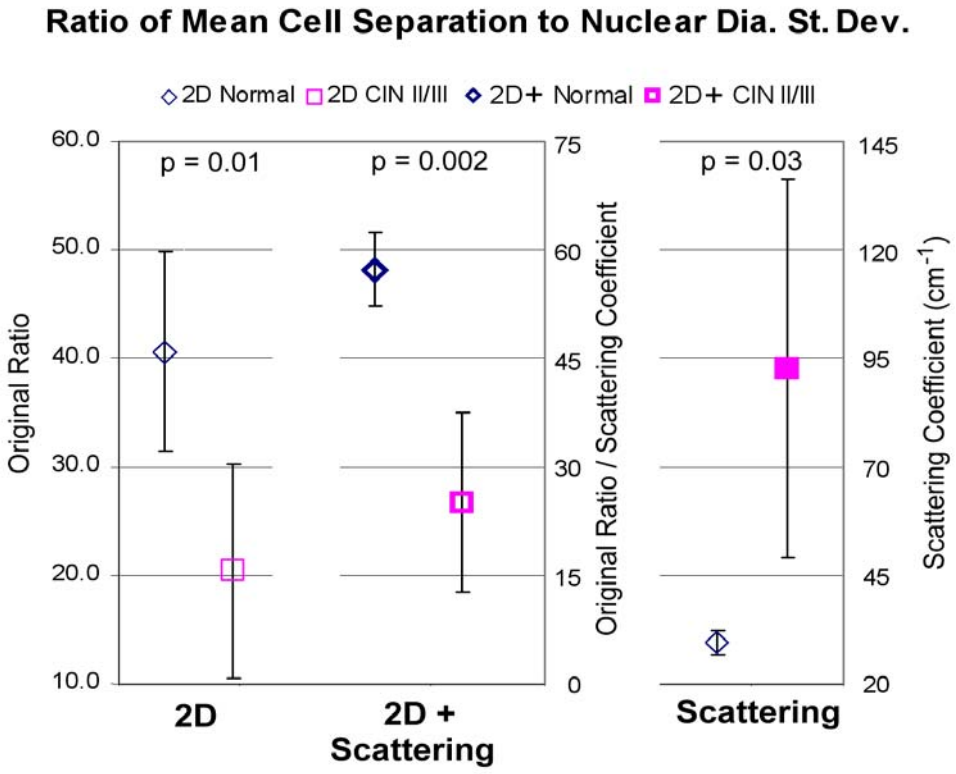

Figure 6.7. Comparison of the mean 2D and 2D + Scattering values for the ratio of mean cell separation to the maximum nuclear diameter standard deviation.

Figure 6.8 compares the statistical significance (1 – p-value) of the differences in the mean morphological features, architectural features, scattering feature and feature combinations for normal and CIN 2/3 samples. Only the features with p-values less than 0.1 are shown. The smallest p-values are obtained when the maximum nuclear diameter standard deviation and cell separation features are used in combination. The combinations using cell separation and nuclear size also performed well with the addition of the scattering information. In all cased where the 2D features are combined with the depth or scattering information, the performance is equal to or greater than the comparable 3D feature. The 2D + Scattering is much more robust than the 2D + Depth for improving the performance of all 2D features. Combinations of scattering coefficient and tissue depth with 3D features are not shown since little improvement is made.

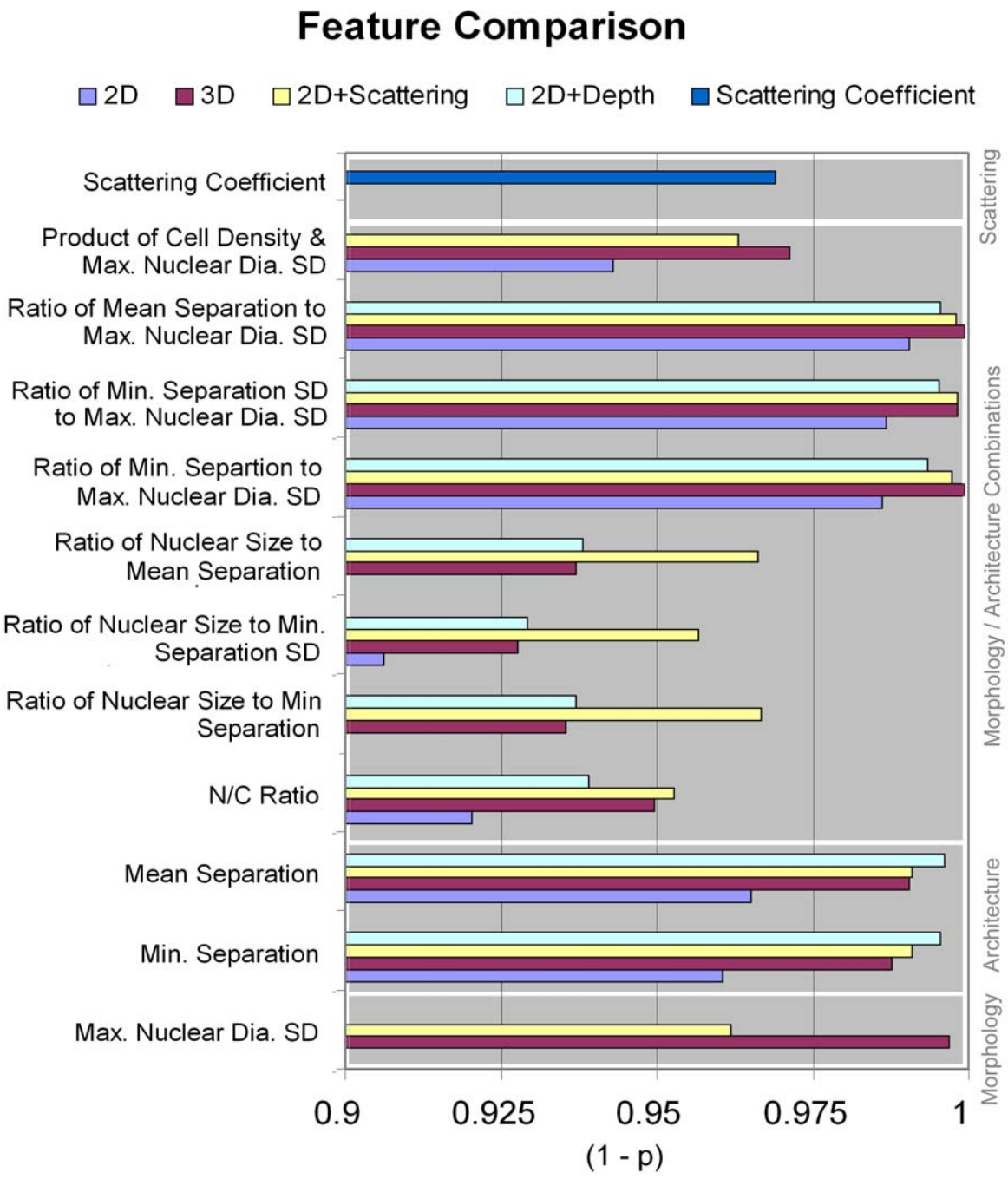

Figure 6.8. Comparison of (1-p) values for various combinations of features.

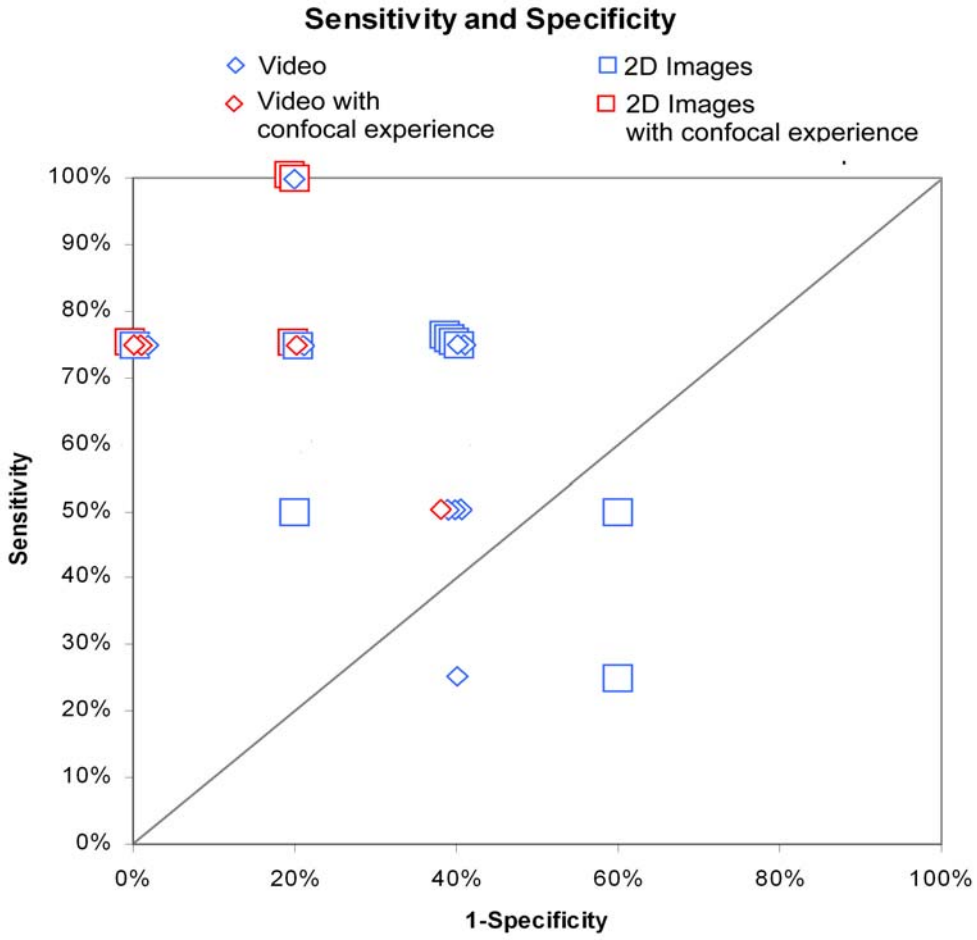

Figure 6.9 Sensitivity and specificity for the diagnoses made by the untrained reviewers. The open squares give the sensitivity and specificity for each reviewer for the 2D images. The open diamonds give the same values for the 3D videos. The red symbols show the sensitivity and specificity for the reviewers with previous confocal imaging experience.

6.3.4 Sensitivity and Specificity

Figure 6.9 shows the sensitivity and specificity values for each of the reviewers for the 2D and 3D confocal image sets. Overall the results indicate no significant improvement using the 3D videos as compared to the 2D images. The average sensitivity and specificity are 71% and 71%, respectively. Improvement

is significant for those with previous experience viewing confocal images, sensitivity and specificity of 88% and 85% respectively

A comparison of the qualitative and quantitative review was performed. Figures 6.10 shows scatter plots of the N/C ratio features used in separating the normal and CIN 2/3 biopsies. The feature is shown for 2D and 2D + Scattering. The data acquired in Chapter 4 was used as a training set with the 2D threshold value (N/C = 0.8) used to separated between normal and CIN 2/3. Another 2D + Scattering threshold was generated using the data in Chapter 4 and the scattering coefficients reported in [78] from the same data set (N/C * Scattering Coefficient = 5.7). Figure 6.11 shows the sensitivity and specificity achieved using these threshold values. For the 2D + scattering N/C ratio, perfect separation was achieved. For comparison the sensitivity and specificity of the untrained reviewer with previous confocal image experience are also shown. No 3D or 2D + Depth features are shown since the training set did not provide the information for generating an independent threshold.

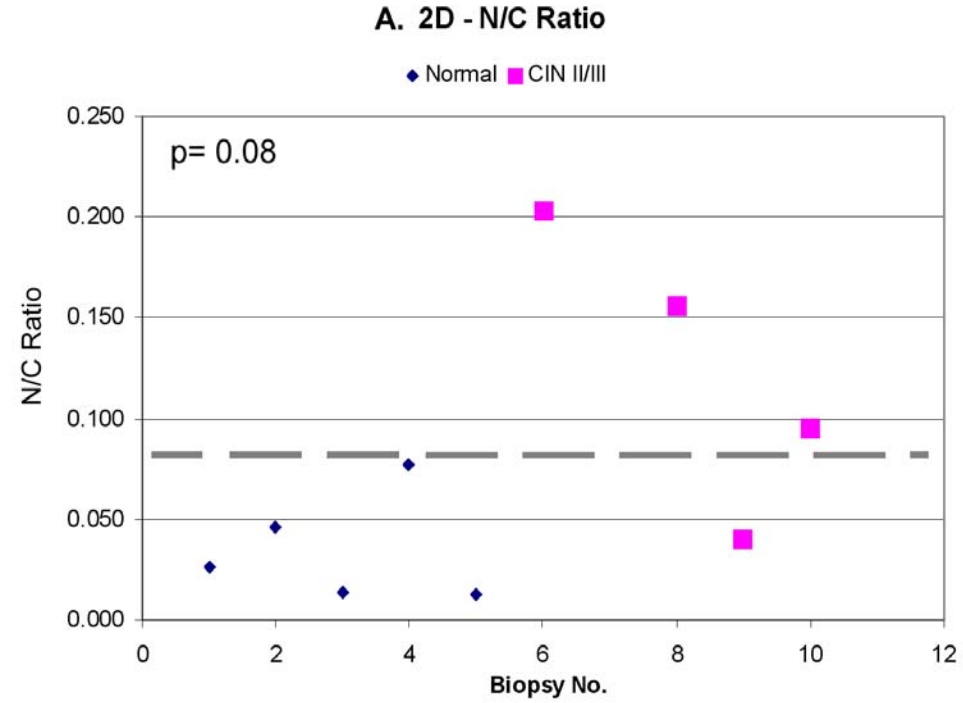
A. 2D - N/C Ratio
Normal
CIN II/III
p= 0.08
N/C Ratio
0.250
0.200
0.150
0.100
0.050
0.000
0
2
4
6
8
10
12
Biopsy No.

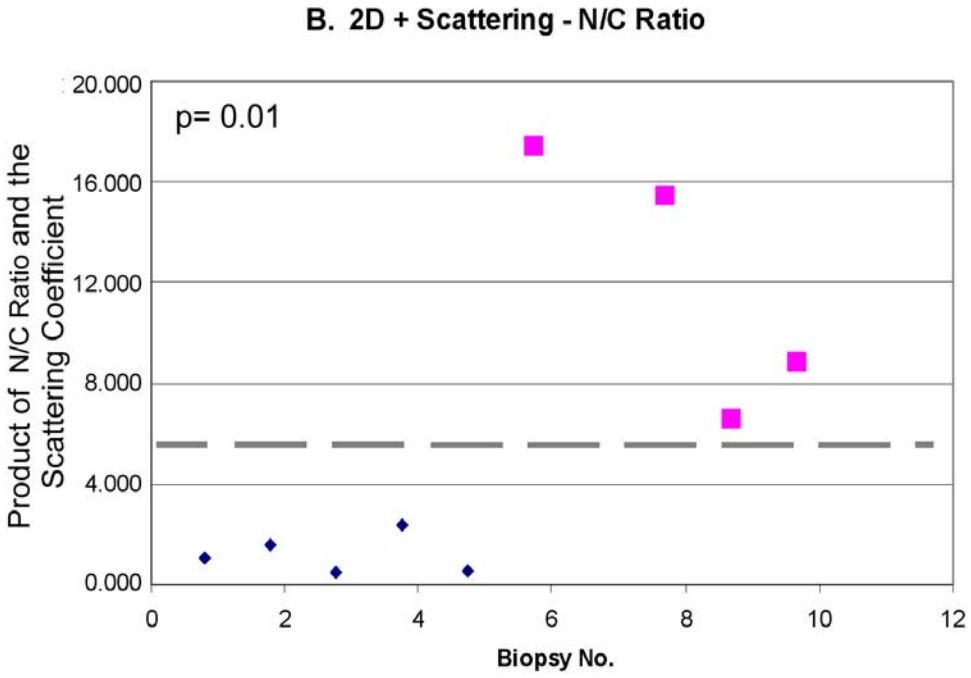
B. 2D + Scattering - N/C Ratio
p= 0.01
Product of N/C Ratio and the Scattering Coefficient
20.000
16.000
12.000
8.000
4.000
0.000
0
2
4
6
8
10
12
Biopsy No.

Figure 6.10. Scatter plots of the 2D and 2D + Scattering features for each biopsy with the threshold value noted (gray line).

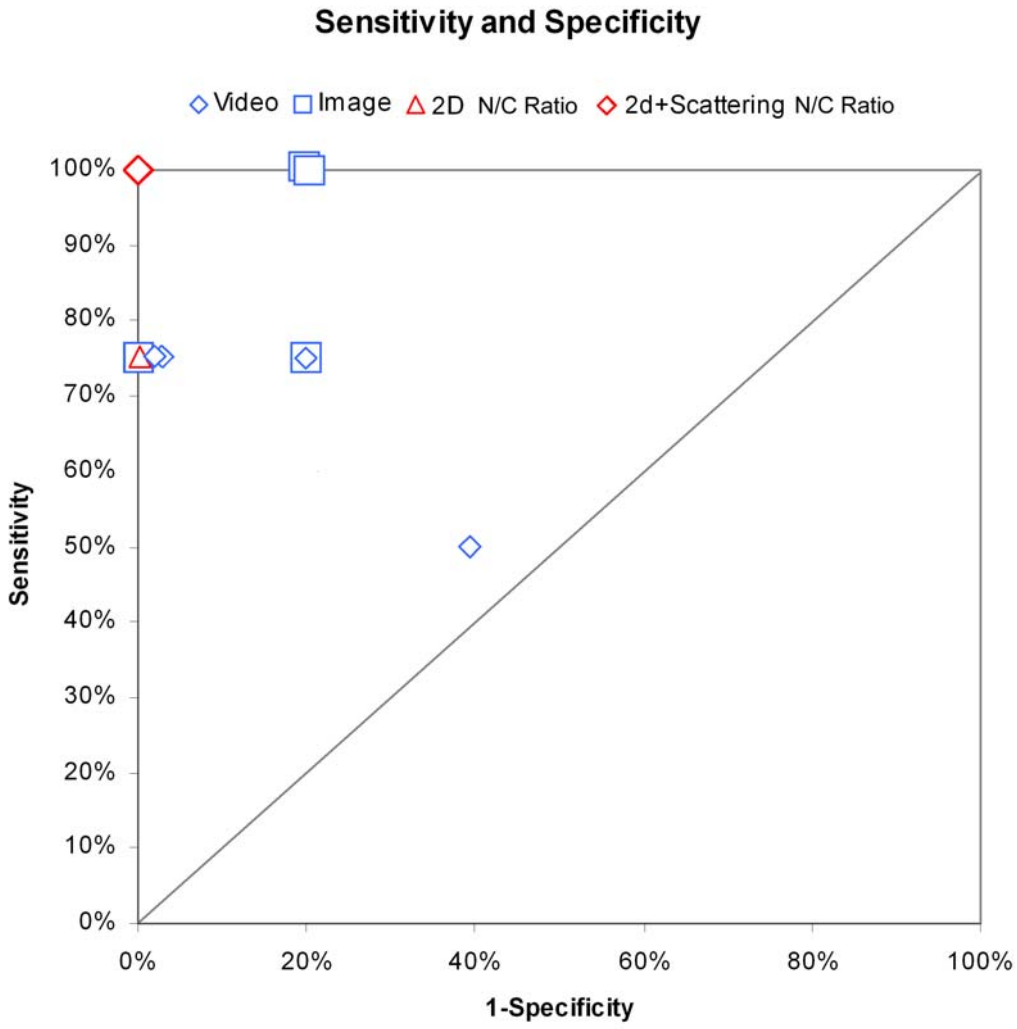

Figure 6.11. Sensitivity and specificity for the N/C ratio extracted from the 2D images (red triangle) and 2D + scattering N/C ratio. The blue symbols show the sensitivity and specificity of the untrained reviewers with previous experience viewing images with the confocal system. The open blue squares give the sensitivity and specificity for each reviewer for the 2D images. The open blue diamonds give the same values for the 3D videos.

6.4 CONCLUSION

The quantitative 3D feature extracted from confocal image stacks show improved separation between normal and CIN 2/3 biopsies compared to the quantitative features captured from single 2D images obtained 50 microns beneath the epithelial surface. However, when 2D image features are compared with one additional piece of information about the epithelium (either the epithelial thickness or the epithelial scattering coefficient), then the 2D features produce separation comparable to the 3D morphology and architecture. The combination of the scattering coefficient and 2D N/C ratio was shown to discriminate between normal and CIN 2/3 with a sensitivity and specificity of 100%. This is an improvement over the 2D N/C ratio alone as reported here and Chapter 4 and trends toward the separation produced by the 3D features. A larger study is suggested to make a valid comparison between the diagnostic ability of the 2D + features and 3D features.

The advantage of the 2D+ approach is that much less image data is required (the 3D data sets require 100-300 times additional storage space) and much less computational effort is required. The use of the scattering coefficient is particularly important since this value can be easily estimated using depth dependent confocal images as described in Chapter 5, without requiring images throughout the entire epithelial thickness. The present system can routinely acquire images throughout the entire epithelial thickness in normal cervical tissue; however, images could be acquired from the entire epithelial thickness in only 3 out of 4 of the CIN 2/3 biopsies because of the increased scattering. The success of the 2D+ depth and 2D + scattering features has important implications for using this precancer detection method in the clinic. Acquisition of the epithelial

thickness or scattering coefficient would require less time than 3D image sets and little additional effort would be required to gain the added information over 2D images alone. The result is improved patient care over 2D images alone at no additional costs and reduced costs compared to the use of 3D image sets.

REFERENCES

[1] Whitte WM, Ragadhyaksha M, Gonzalez S, Fabian RL, Anderson RR. Noninvasive imaging of human oral mucosa in vivo by confocal reflectance microscopy. Laryngoscope 1999; 109:1709-1717.

[2] Rajadhyaksha, M. Grossman, D. Esterowitz, R. H. Webb, and R. R. Anderson, *"In vivo* confocal scanning laser microscopy of human skin: Melanin provides strong contrast," *I. Invest. Dermatol.* vol. 104, pp. 946-52, 1995.

[3] Rajadhyaksha, Gonzalez S, Zavislan J, Anderson RR, Webb RH. In vivo confocal scanning laser microscopy of human skin II: advances in instrumentation and comparison with histology. I Invest Dermatol 1999; 104:946-952.

[4] Drezek R, Collier T, Brookner C, Malpica A, Richards-Kortum R, Follen M, et al. Laser scanning confocal microscopy of cervical tissue, before and after application of acetic acid. Am J of Obstetrics and Gynecology 2000; 182:1135-9.

[5] American Cancer Society Web Page, "Cancer facts and figures – 2004," http://www.cancer.org/docroot/stt/stt_0.asp.

[6] T. Wright, R. Kurman, A. Ferenczy, "Precancerous Lesions of the Cervix" in Pathology of the Female Genital Tract, R. Kurman, Ed., pp. 229-277, Springer-Verlag, New York, 1994.

[7] A. K. Dunn, C. Smithpeter, A.J. Welch, R. Richards-Kortum, "Sources of contrast in confocal reflectance imaging," Applied Optics, vol. 35, no. 19, pp. 3441-6, July 1 1996.

[8] T. Wilson and A.R. Carlini, "Size of the detector in confocal imaging systems," Optics Letters, vol. 12 no. 4 pp. 227-9, April 1987.

[9] K.B. Sung, C. Liang, M. Descour, T. Collier, M. Follen & R. Richards-Kortum, "Near Real Time In Vivo Fiber Optic Confocal Microscopy: Sub-Cellular Structure Resolved," Journal of Microscopy, paper under review.

[10] Collier T, Shen P, de Pradier B, Sung K, Richards-Kortum R. Near real time confocal microscopy of amelanotic tissue: dynamics of aceto-whitening enable nuclear segmentation. Optics Express 2000; 6:40-48. Available from: URL: http://www.opticsexpress.org

[11] D.M. Parkin, P. Pisani, J. Ferlay Estimates of the Worldwide Incidence of Eighteen Major Cancers in 1985. Int. J. Cancer 1993; 54,594-606.

[12] G. Dallen Bach-Hellueg, H. Doulson, *Histopathology of the Cervix Uteri*, (Springer-Verlag New York Inc., 1990).

[13] C. Bertrand and P. Corcuff, *"In vivo* spatio-temporal visualization of the human skin by real time confocal microscopy," Scanning **16**, 150-154 (1994).

[14] P. Corcuff, G. Gonnord, G.E. Pierard, and J. L. Leveque, *"In vivo* microscopy of human skin: A new design for cosmetology and dermatology," Scanning **18,** 351-355 (1996).

[15] B. R. Masters, U. I. Aziz, A. F. Gmitro, J. H. Kerr, T. C. O'Grady, and L. Goldman, "Rapid observation of unfixed, unstained human skin biopsy specimens with confocal microscopy and visualization," L Biomed. Opt. **2**, 437~5 (1998)

[16] V. Jester, P. M. Andrews, W. M. Petroll, M. A. Lemp, and H. D. Cavanaugh, *"In vivo,* real-time confocal imaging," L Electron Microsc. Tech. 18:50-60 (1991).

[17] J. V. Jester, W. M. Petrull, R. M. Garana, M. A. Lemp, and H. D. Cavanaugh, "Comparison *of in vivo* and *ex vivo* cellular structure in rabbit eyes detected by tandem scanning microscopy," I. Microsc. 165: 169-181 (1992).

[18] B. Masters and A. A. Thaer, "Real-time scanning slit confocal microscopy of the *in vivo* human cornea," AppI. Opt. 33: 695-701 (1994).

[19] C. L. Smithpeter, A. K. Dunn, A. I. Welch, and R. Richards-Kortum, "Penetration depth limits of *in vivo* confocal reflectance imaging," AppI. Opt. 37:2749-2754 (1998).

[20] L. Burke, D. Antonioli, B. Durcatman, *Colposcopy Text and Atlas*, (Appleton and Lange., 1991)

[21] J. Thiran and B. Macq, "Morphological Feature Extraction for the Classification of Digital Images of Cancerous Tissues," IEEE Trans. Biomed., 43:1011-1020, (1996)

[22] A. Gmitro and D. Aziz, "Confocal microscopy through a fiber-optic imaging bundle," Opt. Lett. 18, 565-567 (1993).

[23] R. Juskaitis, T. Wilson, and T.F. Watson, "Real time white light reflection confocal microscopy using a fiber-optic bundle," Scanning. 19:15-19 (1997).

[24] T. Dabbs and M. Glass, "Fiber-optic confocal microscope*:* FOCON," Appi. Opt 31:3030-3035 (1992).

[25] L. Giniunas, R. Juskaitis, and S.V. Shatalin, "Endoscope with optical sectioning capability," Appi. Opt. 32:2888-2890 (1993).

[26] D.L. Dickensheets and G.S. Kino, "Micro-machined scanning confocal optical microscope," Opt. Lett. 21:764-766 (1996).

[27] T. Collier, A. Lacy, A. Malpica, M. Follen and R. Richards-Kortum, "Near Real Time Confocal Microscopyof Amelanotic Tissue: Detection of Dysplasia in Ex-Vivo Cervical Tissue." *Academic Radiology*, vol. 9, pp. 504-512, 2002.

[28] Kurman RJ, ed. Blaustein's pathology of the female genital tract, 4th ed. New York, NY: Springer-Verlag, 1994

[29] C. Bertrand and P. Corcuff, *"In vivo* spatio-temporal visualization of the human skin by real time confocal microscopy," Scanning **16**, 150-154 (1994).

[30] P. Corcuff, G. Gonnord, G.E. Pierard, and J. L. Leveque, *"In vivo* microscopy of human skin: A new design for cosmetology and dermatology," Scanning **18,** 351-355 (1996).

[31] B. R. Masters, U. I. Aziz, A. F. Gmitro, J. H. Kerr, T. C. O'Grady, and L. Goldman, "Rapid observation of unfixed, unstained human skin biopsy

specimens with confocal microscopy and visualization," L Biomed. Opt. 2, 437~5 (1998)

[32] V. Jester, P. M. Andrews, W. M. Petroll, M. A. Lemp, and H. D. Cavanaugh, *"In vivo,* real-time confocal imaging," L Electron Microsc. Tech. 18:50-60 (1991).

[33] J. V. Jester, W. M. Petrull, R. M. Garana, M. A. Lemp, and H. D. Cavanaugh, "Comparison *of in vivo* and *ex vivo* cellular structure in rabbit eyes detected by tandem scanning microscopy," I. Microsc. 165: 169-181 (1992).

[34] B. Masters and A. A. Thaer, "Real-time scanning slit confocal microscopy of the *in vivo* human cornea," AppI. Opt. 33: 695-701 (1994).

[35] Smithpeter CL, Dunn AK, Drezek R, Collier T, Richards-Kortum R. Near real time confocal microscopy of cultured amelanotic cells: sources of signal, contrast agents and limits of contrast. J Biom Opt 1998; 3:429-436.

[36] Mitchell MF, Schottenfeld D, Tortolero-Luna G, Cantor SB, Richards-Kortum R. Colposcopy for the diagnosis of squamous intraepithelial lesions: a meta-analysis. Obstetrics and Gynecology 1998; 91:626-31.

[37] Mao L, El-Naggar AK, Papadimitrakopoulou V, Shin DM, Shin HC, Hong WK, et al. Phenotype and genotype of advanced premalignant head and neck lesions after chemopreventive therapy. J National Cancer Institute 1998; 90:1545-51.

[38] J. R. Mourant, I. J. Bigio, J. Boyer, R. L. Conn, T. Johnson, and T. Shimada, "Spectroscopic diagnosis of bladder cancer with elastic light scattering." *Lasers Surg Med*, vol. 17, pp. 350-357, 1995.

[39] Z. Ge, K. T. Schomacker, and N. S. Nishioka, "Identification of colonic dysplasia and neoplasia by diffuse reflectance spectroscopy and pattern recognition techniques." *Appl Spectrosc,* vol. 52, pp. 833-345**,** 1998

[40] F. Koenig, R. Larne, H. Enquist, F. J. McGovern, K. T. Schomacker, N. Kollias, and T. F. Deutsch, "Spectroscopic measurement of diffuse reflectance for enhanced detection of bladder carcinoma." *Urology*, vol. 51, pp. 342-345, 1998.

[41] M. S. Feld, "Spectral pathology using reflected light." In *Biomedical Optical Spectroscopy and Diagnostics*, Optical Society of America, Washington DC, 1998.

[42] G. Zonios, L. T. Perelman, V. Backman, R. Manahoran, M. Fitzmaurice, J. Van Dam, and M. S. Feld, "Diffuse reflectance spectroscopy of human adenomatous colon polyps in vivo." *Appl Optics,* vol. 38, pp. 6628-6637, 1999.

[43] I. J. Bigio, and J.R. Mourant: "Ultraviolet and visible spectroscopies for tissue diagnostics: fluorescence spectroscopy and elasticscattering spectroscopy." *Phys Med Biol*, vol. 42, pp. 803-814, 1997.

[44] R. Glasgold, M. Glasgold, H. Savage, J. Pinto, R. Alfano and S. Schantz, "Tissue autofluorescence as an intermediate endpoint in NMBA-induced esophageal carcinogenesis," *Cancer Letters*, vol. 82, pp. 33-41, Jul., 1994

[45] R. Alfano, A. Pradhan, G. Tang and S. Wahl, "Optical spectroscopic diagnosis of cancer and normal breast tissues," *J. Opt. Soc Am B*., vol. 6 pp. 1015-1023, 1989.

[46] R. Richards-Kortum, and E. Sevick-Muraca, "Quantitative optical spectroscopy for tissue diagnosis." *Annu Rev Phys Chem*, vol. 47, pp. 555-606, 1996.

[47] I. Georgakoudi, B. C. Jacobson, J. Van Dam, V. Backman, M. B. Wallace, M. G. Muller, Q. Zhang, K. Badizadegan, D. Sun, G. A. Thomas, L. T. Perelman, and M. S. Feld, "Fluorescence, reflectance, and light-scattering spectroscopy for evaluating dysplasia in patients with Barrett's esophagus." *Gastroenterology,* vol. 120(7), pp. 1620-9, June, 2001.

[48] J.D. Pitts, R.D. Sloboda, K.H. Dragnev, E. Dmitrovsky and M.A. Mycek, "Autofluorescence characteristics of immortalized and carcinogen-transformed human bronchial epithelial cells," *Journal of Biomedical Optics*.vol. 6, pp. 31-40, Jan., 2001.

[49] F. Koenig, F.J. McGovern, A.F. Althausen, T.F. Deutsch and K.T. Schomacker, "Laser induced autofluorescence diagnosis of bladder cancer," *Journal of Urology*, vol. 156, pp. 1597-601, Nov., 1996.

[50] Z. Haung, H. Zeng, I. Havzavi, D. McLean, and H. Lui, “Rapid near-infrared Raman spectroscopy system for real-time in vivo skin measurements,” *Optics Letters*, vol. 26, pp. 1782-1784, 2001.

[51] A. Mahadevan-Jansen, and R. Richards-Kortum, “Raman spectroscopy for the detection of cancers and precancers.” *J Biomed Optics*, vol.1, pp. 31-70, 1996.

[52] M. Rajadhyaksha, G. Menaker, T. Flotte, P. J. Dwyer, and S. Gonzalez, “Confocal examination of nonmelanoma cancers in thick skin excisions to potentially guide mohs micrographic surgery without frozen histopathology.” *Journal of Investigative Dermatology*, vol.117, pp.1137-43, 2001.

[53] J. Busam, K. Hester, C. Charles, D. Sachs, C. Antonescu, S. Gonzalez, and A. Halpern, “Detection of Clinically Amelanotic Malignant Melanoma and Assessment of Its Margins by In Vivo confocal Scaning Laser Miscroscopy,” *Academic Dermatology*, vol. 137, pp. 923-929, 2001.

[54] M. E. Brezinski, G. J. Tearney, B. E. Bouma, J. A. Izatt, M. R. Hee, E. A. Swanson, J. F. Southern, and J. G. Fujimoto, "Optical Coherence Tomography for Optical Biopsy," *Circulation*, pp. 1206-1213, 1996.

[55] F. I. Feldchtein, V. M. Gelikonov, G. V. Gelikonov, R. V. Kuranov, N. D. Gladkova, A. M. Sergeev, N. M. Shakhova, I. A. Kuznetzova, A. M. Denisenko, and O. S. Streltzova, "Design and Performance of an Endoscopic OCT System for *In Vivo* Studies of Human Mucosa," presented at the Conference on Lasers and Electro-Optics, San Francisco, CA, 1998.

[56] R. Drezek, M. Guillaud, T. Collier, I. Boiko, A. Malpica, C. Macaulay , M. Follen and R. Richards-Kortum, “Light Scattering from Cervical Cells throughout Neoplastic Progression: Influence of Nuclear Morphology, DNA Content, and Chromatin Texture,” submitted to *Biophysical Journal*, 2001.

[57] K. Sokolov, R. Drezek, K. Gossage and R. Richards-Kortum, “Reflectance Spectroscopy with Polarized Light: Is It Sensitive to Cellular and Nuclear Morphology?” *Optics Express*, vol. 5, pp. 302-317, 1999.

[58] W.K. Hong and M.B. Sporn, "Recent advances in chemoprevention of cancer," *Science*. vol. 278, pp. 1073-7, Nov., 1997.

[59] I. Georgakoudi, E. E. Sheets, M. G. Muller, V. Backman, C. P. Crum, K. Badizadegan, R. R. Dasari, and M. S. Feld, "Trimodal spectroscopy for the detection and characterization of cervical precancers in vivo," *American Journal of Obstetrics & Gynecology*. vol. 186(3), pp. 374-82, Mar. 2002.

[60] I. Pavlova, K. Sokolov, R. Drezek, A. Malpica, M. Follen and R. Richards-Kortum, "Microanatomical and Biochemical Origins of Normal and Precancerous Cervical Autofluorescence using Laser Scanning Fluorescence Confocal Microscopy," *Photochemistry & Photobiology,* vol. 77(5), pp. 550–555, 2003.

[61] R. Drezek, C. Brookner, I. Pavlova, I. Boiko, A. Malpica, R. Lotan, M. Follen and R. Richards-Kortum, "Autofluorescence microscopy of fresh cervical-tissue sections reveals alterations in tissue biochemistry with dysplasia," *Photochemistry & Photobiology,* vol. 73(6), pp. 636-41, June 2001.

[62] R. J. Hunter, M. S. Patterson, T. J. Farrell, and J. E. Hayward, "Hemoglobin oxygenation of a two-layer tissue-simulating phantom from time-resolved reflectance: effect of top layer thickness." *Physics in Medicine & Biology*, vol. 47(2), pp.193-208, Jan. 21, 2002.

[63] T. J. Pfefer, K. T. Schomacker, M. N. Ediger and N. S. Nishioka, "Multiple-fiber probe design for fluorescence spectrocscopy in tissue," *Applied Optics*, vol. 41, pp. 4712-4721, Aug., 2002.

[64] B.W. Pogue and G. Burke, "Fiber-optic bundle design for quantitative fluorescence measurements from tissue," *Applied Optics*, vol. 31, pp. 7429-7436, Nov., 1998.

[65] L. Quan and N. Ramanujam, "Relationship between depth of a target in a turbid medium and fluorescence measured by a variable=aperture method," *Optics Express*, vol. 27, pp. 104-106, Jan., 2002.

[66] W. Cheong, S. Prahl, and A. Welch, "A Review of the Optical Properties of Biological Tissues." *IEEE J of Quantum Electronics*, vol. 26, pp. 2166-2185, 1990.

[67] J.W. Pickering, S.A. Prahl, N. van Wierington, J.F. Beek, H.J.C.M. Sterenborg and M..J.C. van Gemert, "Double-integrating-sphere system for measuring the optical properties of tissue," *Applied Optics,* vol. 33, pp. 399-410, 1993.

[68] S.A. Prahl, M..J.C. van Gemert and A.J. Welch, "Determining the optical properties of turbid media by using the adding-doubling method," *Applied Optics,* vol. 32, pp. 559-568, 1993.

[69] T. Foster and E. Hull, "Optical Tomography and Spectroscopy of Tissue: Theory, Instrumentation, Model and Human Studies II," *Proc. Of SPIE-Intern. Soc. Opt Eng*., vol. 2979, pp. 337, 1997.

[70] S. Lin, L. Wang, S. Jacques and F. Tittel, "Measurement of tissue optical properties using oblique incidence optical fiber reflectometry," *Applied Optics* vol. 36, pp. 136-143, 1997.

[71] D. Arifler, M. Guillaud, A. Carraro, A. Malpica, M. Follen and R. Richards-Kortum, "Light Scattering from normala and dysplastic cervical cells at defferent epithelial depths: finite-difference time-domain modeling with a perfectly matched layer boundary condition**,"** *J. Biomedical Optics*, vol. 38, paper under review.

[72] R. Bays, G. Wagnieres, D. Robert, D. Braichotte, J. Savory, P. Monnier and H. van den Bergh, "Clinical Determination of tissue optical properties by endoscopic spatially resolved reflectrometry," *Applied Optics,* vol. 35, pp. 1756-1766, Apr. 1996.

[73] R. Hornung, T.H. Pham, K.A. Keefel, M.W. Berns, Y. Tadir and B.J. Tromberg, "Quantitative near-infrared spectroscopy of cervical dysplasia in vivo," *Human Reproduction,* vol. 14, pp. 2908-2916, Nov. 1999.

[74] S.K. Sung, D. Arifler, R. Drezek, M. Follen, R. Richards-Kortum, "Analytical Model to Describe Fluorescence Spectra of Normal and Preneoplastic Epithelial Tissue: Comparison with Monte Carlo Simulations and Clinical Measurements", Journal of Biomedical Optics, vol. 9(3) pp. 511-522, May/June 2004.

[75] J. Qu, C. MacAuley, S. Lam, and B. Palcic, "Optical Properties of normal and carcinomatous bronchial tissue," *Applied Optics,* vol. 33, pp. 7397-7405, Nov., 1994.

[76] M. Kempe, W. Rudolph, and E. Welsch, "Comparative Study of Confocal and Heterdyne Microscopy for Imaging Through Scattering Media." *Journal of the Optical Society of America*, vol. 13, pp. 46-52, 1996.

[77] J. Schmitt, A. Knuttel, and M. Yadlowsky, "Confocal Microscopy in Turbid Media" *Journal of the Optical Society of America,* vol. 11, pp. 2226-2235, 1994.

[78] T. Collier, D. Arifler, A. Malpica, M. Follen, R. Richards-Kortum, "Determination of the Epithelial Tissue Scattering Coefficient Using Confocal Microscopy." Selected Topics in Quantum Electronics, vol. 9, pp. 307-313, 2003.

[79] B. Luck, A. Bovic, R. Richards-Kortum, "Segmenting cervical epithelial nuclei from confocal images Gaussian Markov random fields", Image Processing, 2003. Proceedings. 2003 International Conference on, vol. 2 , pp. 14-17 Sept. 2003.

[80] J.R. Mourant, T. Fuselier, J. Boyer, T. M. Johnson, and I. J. Bigio, "Predictions and measurements of scattering and absorption over broad wavelength ranges in tissue phantoms," *Applied Optics*, vol. 36, pp. 949-957, Feb. 1997.

[81] A. Zoumi, A. Yeh, and B. J. Tromberg, "Imaging cells and extracellular matrix *in vivo* by using second-harmonic generation and two-photon excited fluorescence," *Proc. Of the Nat. Acad. of Am.,* vol. 99, pp. 11014-11019, Aug., 2002.

[82] J. Key, E.R. Davies, R.C. Jackson and P.N. Wells, "Optical attenuation characteristics of breast tissues at visible and near-infrared wavelengths," *Physics in Medicine and Biology*, vol. 36, pp. 579-590, May 1991.

[83] V.G. Peters, D.R. Wyman, M.S. Patterson and G.L. Frank, "Optical properties of normal and diseased human breast tissues in the visible and near infrared," *Physics in Medicine and Biology*, vol. 35, pp. 1317-1334, Sep., 1990.

[84] C. R. Simpson, M. Kohl, M. Essenpreis and M. Cope, "Near-infrared optical properties of *ex vivo* himan skin and subcutaneous tissues measured using the Monte Carlo inversion technique," *Physics in Medicine and Biology*, vol. 43, pp. 2465-2478, Sep., 1998.

[85] T.L. Troy and S.N. Thennadil, "Optical properties of human skin in the near infrared wavelength range of 1000 to 2200 nm," *J. Biomedical Optics*, vol. 6 pp. 167-176, Apr,. 2001.

[86] M. Guillaud, D. Cox, K. Adler-Storthz, A Malpica, G. Staerkel, J. Matisic, D. Van Niekerk, N. Poulin, M. Follen, C. MacAulay, "Exploratory Analysis of Quantitative Histopathology of Cervical Intraepithelial Neoplasia: Objectivity, Reproducibility, Malignancy-Associated Changes, and Human Papillomavirus", Cytometry, vol. 60A, pp. 81-89, 2004.

[87] C. Sowter, P. Bertolino, "Histometry and the H.O.M.E. concept: An aid to the grading of intra-cervical neoplasia?", Analytical Cellular Pathology, vol. 9, pp. 269-279, 1995.

VITA

Thomas Glenn Collier received his Bachelor of Architecture in 1987 from the University of Texas at Austin. He worked as a registered architect until reentering the University of Texas where he received his Masters of Electrical Engineering in 2000. He continued at the University of Texas at Austin to pursue a Doctorate in Electrical Engineering. His thesis research explores the use of confocal microscopy as a tool for diagnosing precancers.

Perminant Address: 4705 Ramsey Ave. Austin, Texas 78756

This dissertation was typed by the author.